END

DATE
FILMED

7 80

DTIC

1.0

1.1

1.25

4.5
5.0
5.6
6.3

2.8

3.2

36

40

1.4

2.5

2.2

2.0

1.8

1.6

MICROCOPY RESOLUTION TEST CHART
NATIONAL BUREAU OF STANDARDS 1963 A

REPORT DOCUMENTATION PAGE		READ INSTRUCTIONS BEFORE COMPLETING FORM
1. REPORT NUMBER	2. GOVT ACCESSION NO. AD-A085 753	3. RECIPIENT'S CATALOG NUMBER
4. TITLE (and Subtitle) LOCALIZED DEFORMATION AND FRACTURE OF TRANSPARENT CERAMICS		5. TYPE OF REPORT & PERIOD COVERED Technical report
		6. PERFORMING ORG. REPORT NUMBER CR80-758
7. AUTHOR(s) W. F. Adler and T. W. James		8. CONTRACT OR GRANT NUMBER(s) N00014-76-C-0744
9. PERFORMING ORGANIZATION NAME AND ADDRESS Effects Technology, Inc. 5383 Hollister Avenue Santa Barbara, CA 93111		10. PROGRAM ELEMENT, PROJECT, TASK AREA & WORK UNIT NUMBERS Project No. 471 (NE 032-565)
11. CONTROLLING OFFICE NAME AND ADDRESS Office of Naval Research 800 North Quincy Street Arlington, VA 22217		12. REPORT DATE Mar 80
		13. NUMBER OF PAGES 64
14. MONITORING AGENCY NAME & ADDRESS(if different from Controlling Office)		15. SECURITY CLASS. (of this report) Unclassified
		15a. DECLASSIFICATION DOWNGRADING SCHEDULE

16. DISTRIBUTION STATEMENT (of this Report)

Approved for public release; distribution unlimited.

17. DISTRIBUTION STATEMENT (of the abstract entered in Block 20, if different from Report)

William F. Adler
Timothy W. James

18. SUPPLEMENTARY NOTES

19. KEY WORDS (Continue on reverse side if necessary and identify by block number)

water drop impingement, impact, ceramics, fracture,
calcium fluoride, zinc sulfide   ETI-CR 80-758

20. ABSTRACT (Continue on reverse side if necessary and identify by block number)

The objective of this research is to understand and model the deformation and
fracture response of materials exposed to water drop collisions. Due to the
inherent complexity of the erosive response of materials exposed to a multiple
water drop environment, this investigation concentrated on a very idealized
water drop impact condition: the normal impact of a spherical water drop on
a plane surface. Impact experiments were conducted in a specially designed
ballistic range facility capable of producing spherical water drop impacts

DD FORM 1473   EDITION OF 1 NOV 65 IS OBSOLETE
1 JAN 73

405842

Abstract (continued)

on materials at impact velocities from 200 to 850 ms^{-1}. A reproducible, controlled, and well-characterized impact condition is necessary if an accurate assessment of the material's response is to be established and this requirement has been satisfied within this program.

Significant advances have been made in understanding the mechanics of water drop impacts on materials and the sequence of events taking place during the collision process which relates directly to the form of the fractures produced in polycrystalline zinc sulfide. Measurements of the identifiable features of the water drop impact damage in zinc sulfide were made and correlated with the results from the available analyses pertaining to the form of the interfacial pressure distribution, the onset of lateral outflow jetting, and the general form of the subsurface fracture patterns.

In addition to accurately characterizing water drop impact damage in materials, two alternative methods were investigated for simulating the effects of water drop collisions: water jets and nylon beads (or soft body) collisions. Both simulations offer flexibility in the specimen geometry since the impacting mass is propelled against a stationary target. The damage on zinc sulfide produced by nylon bead impacts compared favorably with that due to water drop collisions. The potential exists for establishing equivalence relations for simulating the primary features of water drop impact damage in selected classes of materials using soft polymeric beads. The impact damage produced on zinc sulfide by well characterized water jet collisions was found to display significant deviations from that due to water drops.

The water drop impact damage on single crystal and polycrystalline calcium fluoride was also investigated. Some general observations are made with regard to the form of the fractures in extruded, hot-pressed, and press-forged calcium fluoride.

TABLE OF CONTENTS

THIS PAGE INTENTIONALLY BLANK

LIST OF ILLUSTRATIONS

LIST OF ILLUSTRATIONS (continued)

iv

LIST OF TABLES

1.0 INTRODUCTION

Significant advances have been made in understanding the mechanics of water drop impacts on materials and the sequence of events taking place during the collision process which relates directly to the form of the fractures produced in polycrystalline zinc sulfide. Experiments were carried out in the ETI liquid drop impact facility which is unique with regard to the production and characterization of spherical water drop impacts for velocities ranging from 200 to 850 ms^{-1}. Considerable attention has been devoted to the test procedure in order to assure that the experimental results are representative of the idealized models used for analyzing the impact event and to describe the damage within the target material.

Using zinc sulfide as the target material, measurements have been made of the onset of circumferential fractures which define the boundary of the central undamaged zone (Adler, 1979), the location of the maximum in the peak pressure distribution generated on the water drop/target interface, and representative dimensions for the dominant subsurface fractures which have been identified. The general form of the subsurface fracture patterns have been interpreted in terms of the transient stresses generated by the impact. The available analyses and experimental data appear to be reasonably correlated.

In addition to accurately characterizing water drop impact damage in materials, two alternative methods have been investigated for simulating the effects of water drop collisions: water jets and nylon beads (or soft body) collisions. Both simulations offer flexibility in the specimen geometry since the impacting mass is propelled against a stationary target. These simulation procedures provide the possibility for investigating the effects of water drop impacts on fabricated components, to conduct tests at elevated temperatures, and to provide test bars for residual strength measurements. The nylon bead collisions can be used to gain understanding of water drop impacts from 1000 to above 2000 ms^{-1}. However

1

water jet impacts which would simulate water drop collisions for reasonable drop sizes (on the order of 1 mm) require extremely small orifice diameters beyond 600 ms^{-1}, so from a pragmatic viewpoint the water jet may not be appropriate for impact velocities above 600 ms^{-1}.

Well-characterized water jets were found to produce considerably less correlation with the deformation and fracture damage on zinc sulfide due to water drop collisions than nylon bead impingement. There is reasonable potential for establishing equivalent conditions for simulating the primary features of water drop impact damage using soft polymeric beads.

Magnesium oxide and polymethylmethacrylate were also impacted with nylon beads. Polymethylmethacrylate showed distinctly different deformation and fracture patterns than the water drop impacts which have been studied extensively (Adler and James, 1979). The nylon bead impacts on magnesium oxide were significantly less damaging than water drop collisions based on equivalent kinetic energy. It is thus seen that the correspondence between water drop and nylon bead impacts observed for small-grained zinc sulfide may not be a universal reiation but will be true for particular classes of materials yet to be identified.

The water drop impact damage on single crystal and polycrystalline calcium fluoride was also investigated. Some general observations are made with regard to the form of the fractures in extruded, hot-pressed, and press-forged calcium fluoride.

2.0   ANALYSIS OF WATER DROP IMPACTS ON ZINC SULFIDE

Spherical water drop impact damage in zinc sulfide has been examined in considerable depth for impact velocities from 200 to over 800 ms^{-1}. The excellent quality of the spherical water drop impact conditions achieved in the ETI liquid drop impact facility (Adler and James, 1979) made it possible to quantify the extent of the damage and to refine the prevailing concepts pertaining to the mechanics of water drop impingement (Adler, 1979). Chemically vapor deposited (CVD) zinc sulfide was selected for the target material, since its grain size is small enough that the material response can be considered to be that of a homogeneous, isotropic material. The impact behavior can therefore be evaluated in terms of an axisymmetric analysis. In addition its fracture strength and rigidity are such that negligible to very intense fractures can be achieved over the range of water drop impact conditions available in the impact facility. The general properties of CVD zinc sulfide are summarized in Table 2.1.

The general features of water drop impact damage on zinc sulfide are shown in Fig. 2.1 and 2.2. The cross sectional view in Fig. 2.2a shows the fracture depths increase fairly uniformly outside the central undamaged zone: an excellent example is shown on the left hand side of Fig. 2.2 a. What is most striking in the cross section is the two distinct forms of dominant fractures. The fractures in the inner region tend to approach the surface at shallow angles: these will be referred to as Type I fractures. The second dominant fracture occurs at larger radial distances and is characterized by a very steep angle of approach with the impact face and reversed curvature. These will be designated Type II fractures.

The surface contour through the center of the impact site in Fig. 2.2b shows a depressed annulus similar to that found on the surface of polymethylmethacrylate but of considerably smaller depth (Adler and

3

Table 2.1. Properties of CVD Zinc Sulfide[*]

Density	4090 kg/m^3
Grain size[**]	2 - 5 μm in growth plane; 9 to 30 μm (columnar grains) in growth direction
4-Point Bend Strength	100.8 MPa (14.6 ksi)
K_{IC}[†]	0.67 MPa $m^{1/2}$ (609 psi $\sqrt{in}$)[††]
Knoop Hardness (100 g load)	239 kg/mm^2 (growth plane)
Young's Modulus	74.1 GPa (10.7 x 10^6 psi)
Poisson's Ratio	0.30 (in plane of plate) 0.35 (in growth direction)
Calculated Dilatational Wave Velocity	4,960 ms^{-1}
Calculated Distortional Wave Velocity	2,600 ms^{-1}

---

[*]Taken from Wimmer (1979).

[**]Measured for material used in this investigation

[†]Crack propagation parallel to columnar grains

[††]It should be noted that Evans and Wilshaw (1976) report K_{IC} = 1 MPa $m^{1/2}$ and Shockey, et al. (1977), found K_{IC} = 0.75 MPa $m^{1/2}$
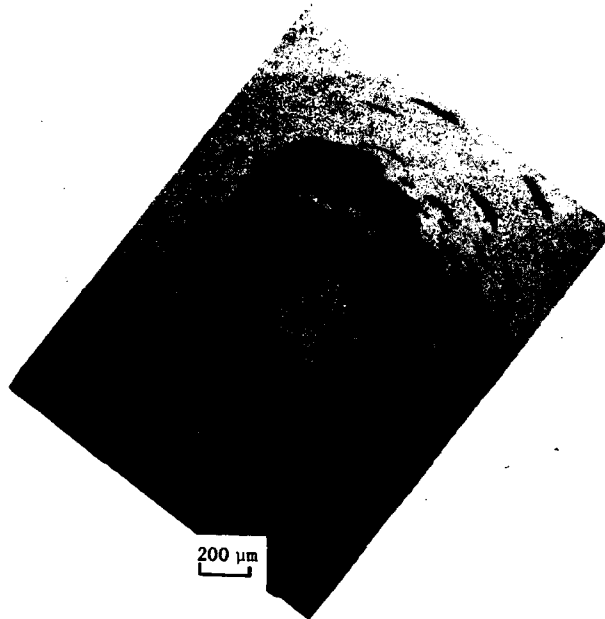
(a) Extent of circumferential fractures shown in
transmitted light illumination.

(b) Etched surface showing actual
radius of central undamaged
zone. Transmitted light
illumination.
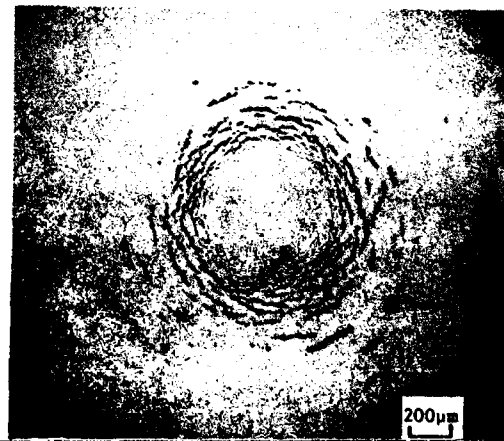
(c) Circumferential fractures
viewed in reflected light
illumination.

Figure 2.1.   General appearance of water drop impact damage
on CVD zinc sulfide.
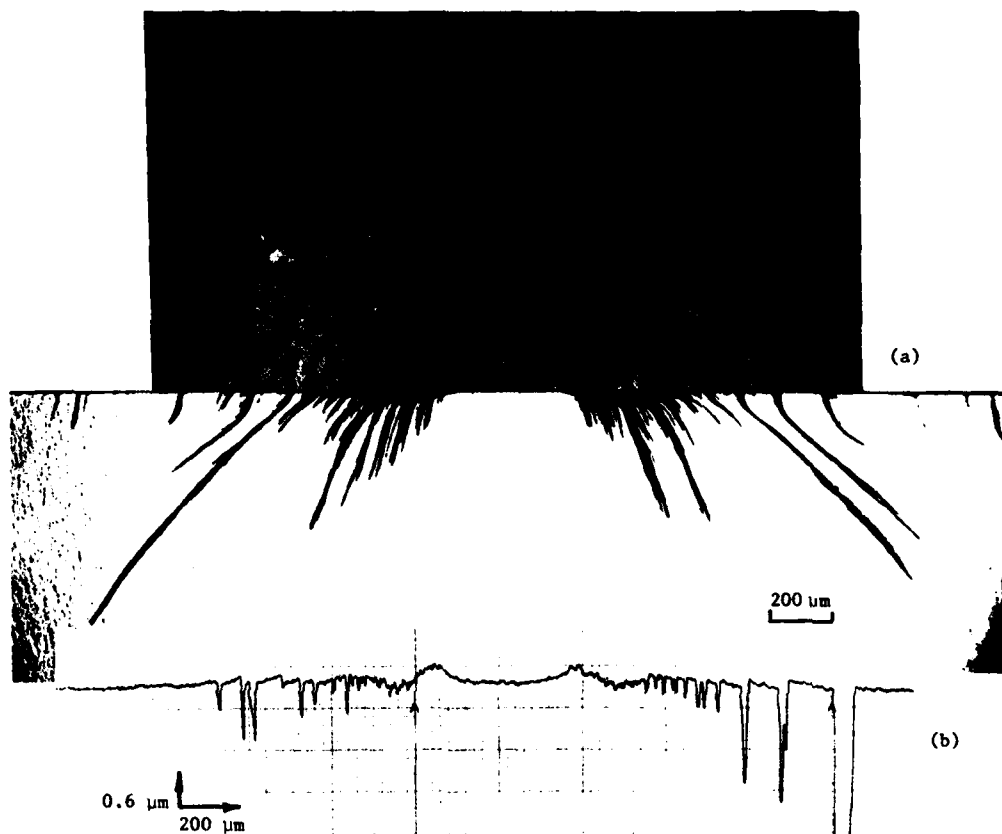
(a) Circumferential fractures seen in reflected light illumination
with subsurface fractures on thin section through center of
impact. Note the increasing level of radial outflow damage
with distance from the center of impact.

(b) Surface profile along center line of impact damage.

Figure 2.2. Impact damage on zinc sulfide due to a 2.30 mm
water drop impacting at 540 ms^{-1}.

James, 1979). The radial locations for the dominant fractures as well as the radius for the onset of the circumferential fractures forming the periphery of the central undamaged zone are clearly seen in Fig. 2.2. These characteristic fractures and deformations are manifestations of the water drop/target interaction. A fairly complete description of the sequence of events taking place during the collision of a spherical water drop with a zinc sulfide target can now be constructed using profilometer traces of the impact surface, cross sectional views of the internal fracture patterns, and analyses of the drop deformations and the response of the target material. The general analytical relations available for understanding the water drop/target interaction will be developed in this section. The quantitive experimental results summarized in Section 3.1 will be compared with these analytical relations.

2.1   KINEMATICS

The sequence of events which take place during the water drop impact are as follows. When a spherical water drop of radius r_o strikes a rigid surface at velocity v_o , the radius of the contact zone, a, increases according to the relation

$$a(t) = \left[2r_o v_o t - (v_o t)^2 \right]^{1/2} \tag{2.1}$$

$$\approx \left(2r_o v_o t \right)^{1/2} \tag{2.2}$$

where t is the time elapsed from the initial contact. The relation in Eq.(2.1) is based on the assumption the drop remains spherical which is valid during the initial stages of the loading process. The approximation in Eq.(2.2) is applicable as long as (a/r_o) $\le$ 0.5 (Adler, 1977).

The rate of expansion of the contact zone is

$$\dot{a}(t) = \frac{v_o(r_o - v_o t)}{a(t)} \tag{2.3}$$

7

The initial rates of radial expansion are quite high but decrease essentially as $t^{-1/2}$. Assuming the surface displacements are small for a hard, elastic target, the rigid surface relations will be equally applicable for a deformable target material. Now stress waves are generated in the elastic half-space (target) at the same time a compression wave propagates into the water drop. As the contact zone velocity decreases, a dilatational, or compression, wave with a characteristic velocity C_ℓ will separate from the contact zone and propagate the effects of the impact into the elastic half-space. This will be followed by the separation of a distortional, or shear, wave from the contact zone with a characteristic velocity C_s, and a Rayleigh wave subsequently propagates along the surface at a velocity C_R which is slightly less than C_s. These wave velocities are defined by

$$C_\ell^2 = \left(\frac{E}{\rho}\right)\left(\frac{1-\nu}{(1+\nu)(1-2\nu)}\right) \tag{2.4}$$

$$C_s^2 = \left(\frac{E}{\rho}\right)\left(\frac{1}{2(1+\nu)}\right) \tag{2.5}$$

where E is Young's modulus, ν the Poisson's ratio, and ρ the density of the medium.

The time and radial distance at which the longitudinal and shear waves separate from the contact zone can be found by equating the velocity of the contact zone, $\dot{a}(t)$, in turn to the longitudinal wave speed for zinc sulfide, $C_\ell = 4.96$ mm/μs, and to the shear wave speed, $C_s = 2.60$ mm/μs. Introducing the first condition,

$$\dot{a} = C_\ell , \tag{2.6}$$

8

into Eq.(2.3) in conjunction with Eq.(2.1) yields

$$v_o t^*/r_o = 1 - \left[1 + (v_o/C_\ell)^2\right]^{-1/2} \tag{2.7}$$

and

$$a^*/r_o = (v_o/C_\ell)\left[1 + (v_o/C_\ell)^2\right]^{-1/2}. \tag{2.8}$$

The asterisks denote the specific values of the contact radius and time
which satisfy Eq.(2.6). A similar result is found for the shear wave.

The transient stresses in the target associated with these stress
waves vary both with respect to locations within the target and time. It
is difficult to conveniently describe the temporal and spatial evolution
of the stress states in the elastic target. Knowledge of the stresses
which develop is important in understanding the onset and propagation of
fracture in the target. The calculation of the transient stresses in the
half-space will be addressed after consideration is given to the magnitude
and form of the impact pressures generated at the water drop/target
interface.

2.2   IMPACT PRESSURE

The pressure distribution applied to the target's surface due to
the impacting water drop has been investigated for some time. However
the published results have been re-examined. The peak pressure distri-
bution as a function of the radial coordinate is generally reported in
the experimental literature. Recent experimental determinations indicate
peak pressures of $2.5\,\rho_w C_w v_o$ (Rochester and Brunton, 1979) where ρ_w
is the density and C_w is the compressional wave speed for water. On
the other hand the temporal and spatial pressure distributions determined
from finite difference computations indicate that the peak pressures are
only achieved for very short time durations and over a quite narrow radial
dimension (Hwang, 1975; Rosenblatt, et al., 1977). Rosenblatt and his
associates (1976, 1977) provided results for a very fine computational

9

mesh during the initial stages of the collision process. This computation
revised the initial form of the evolving pressure distribution (Rosenblatt,
et al., 1976) and due to the small grid dimensions is believed to be the
most reliable numerical computation available. These numerical results
compare favorably with the experimental results (Rochester and Brunton,
1979) both with regard to the magnitude of the maximum in the peak
pressure and its radial location.

The following observations are drawn from the limited numerical
results reported by Rosenblatt and his co-workers: primarily for a 1 mm
water drop impact at 335 ms^{-1}.

> During the initial loading period the pressure distribu-
> tion is fairly uniform except for a sharp rise in
> pressure in the vicinity of the boundary of the
> contact zone.

> The magnitude of the uniform portion of the impact pres-
> sure approximates the water hammer pressure $(\rho_w C_w v_o)$
> while the peak pressure reaches a maximum value of
> 2.7 times the water hammer pressure.

> The maximum duration of the pressure spike is less than
> 5 ns.

> The maximum in the peak pressure distribution occurs
> when $\dot{a} = C_w$.

The early time pressure distributions computed by Rosenblatt,
et al., are shown in Fig. 2.3 and 2.4. A curve approximating the radial
variation in the peak pressures is superposed on the calculated values.
The peak pressures are seen to have an initial value equal to the Hugoniot
pressure, $p = \rho_w U_w v_o$ where U_w is the shock velocity in water, but the
pressure distribution is quite uniform and has an average value close to
the water hammer pressure.
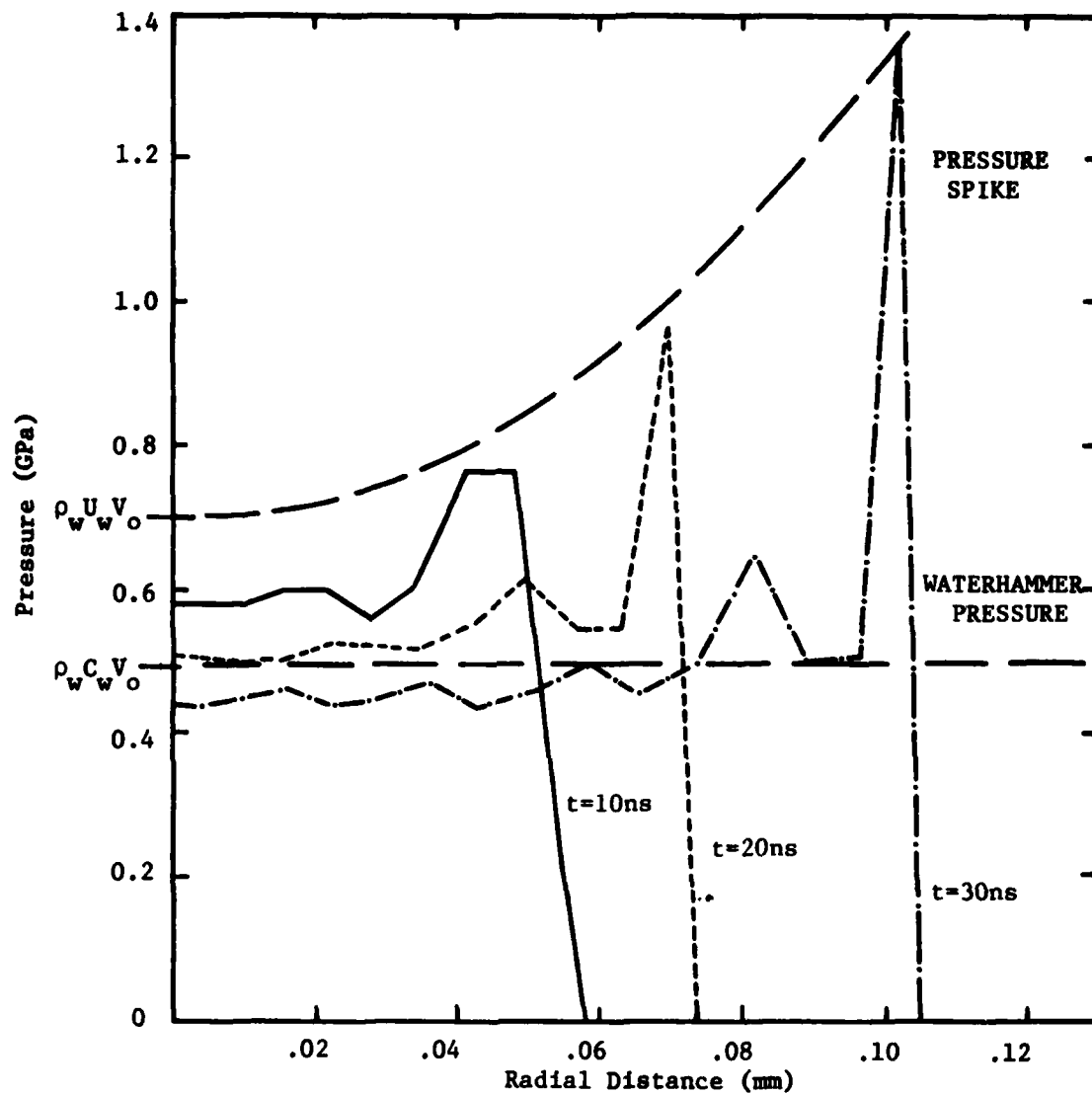
Figure 2.3. Pressure as a function of radial distance for a 1 mm
water drop impacting a rigid surface at 335 ms^{-1}
(adapted from Rosenblatt, et al., 1977). The locus
of the peak pressure is indicated rising from the
Hugoniot pressure to twice the Hugoniot pressure.
The average pressure is seen to be close to the water
hammer pressure.
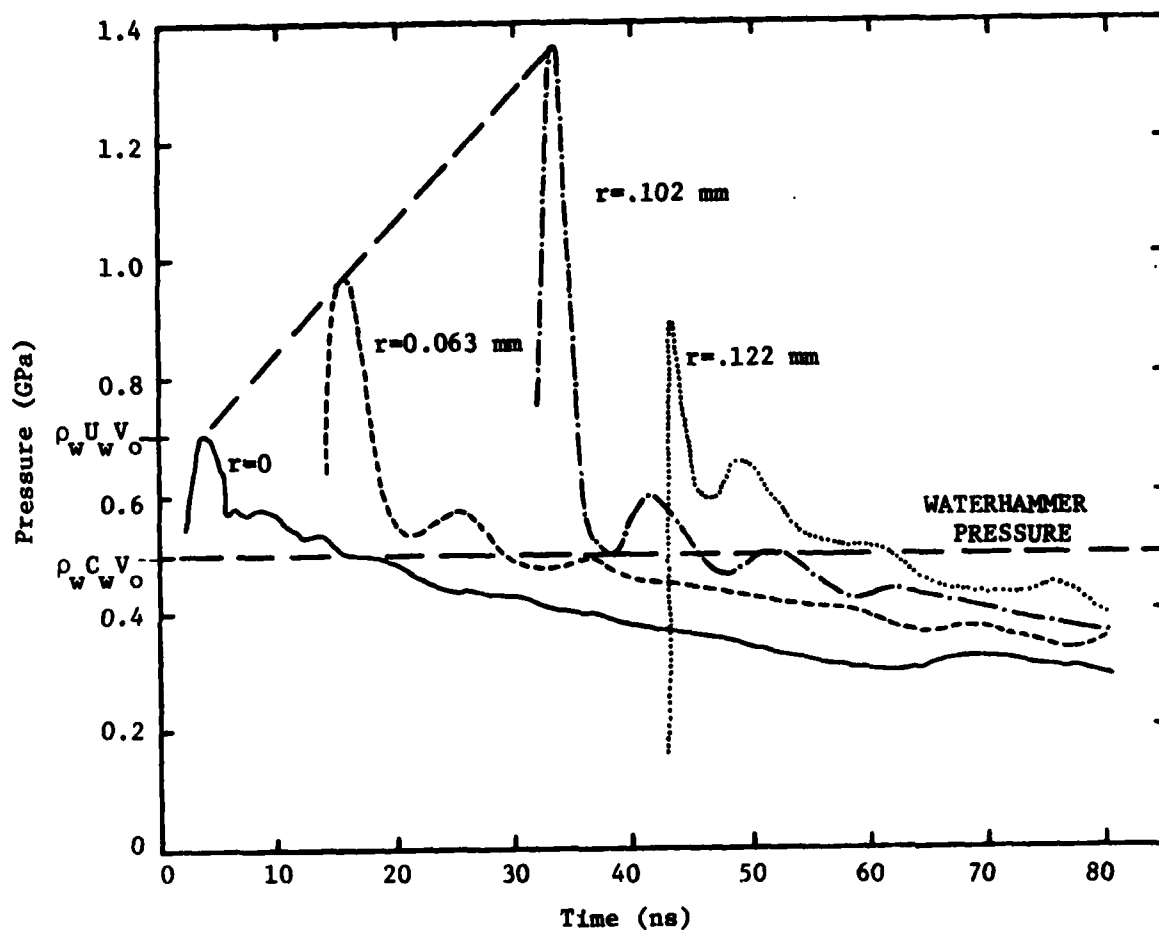
Figure 2.4. Pressure as a function of time for a 1 mm water drop impacting a rigid surface at 335 ms^{-1} (from Rosenblatt, et al. 1977).

12

Hwang's numerical results (Hwang, 1975) also show a sharp rise in
the applied pressure in the vicinity of the periphery of the expanding
contact zone. However Hwang's solution indicates the magnitude of the
average and peak pressures are generally below the water hammer pressure
and the location of the maximum in the peak pressure occurs at a consider-
ably larger radial distance than found in Rosenblatt's finite difference
computations.

These observations pertaining to the numerical computations are
advanced to support our hypothesis that the effect of the pressure spike
is of second order in the stress calculations for an elastic half-space.
The impact pressure can be then adequately represented by a spatially
uniform pressure distribution whose magnitude equals the water hammer
pressure. It will be assumed that the specified pressure distribution
will prevail at least until the radius of the contact zone reaches a
value determined from the condition that $\dot{a} = C_w$. This condition defines
the radial dimensions for which pressure release occurs which would also
imply lateral outflow jetting is initiated (Adler, 1979). Although only
one impact condition has been considered, it will be assumed that the
observations pertaining to the impact pressure are valid for an extended
range of impact velocities.

The various parameters associated with the conditions described
in the previous discussions are summarized in Fig. 2.5 and 2.6 for future
reference. Figure 2.5 indicates the magnitude of the Hugoniot and water
hammer pressures as a function of impact velocity for a zinc sulfide tar-
get material. The impact pressures for a rigid surface are also shown for
comparison. The plots in Fig. 2.6 show the location of the boundary of
the contact zone when various conditions are imposed: separation of the
compression wave, separation of the shear wave, and the location of the
maximum in the peak pressure distribution. The times at which these
radial distances are reached are also given. The times and radial dis-
tances are computed from equations of the general form indicated in
Eq.(2.7) and (2.8). The condition $\dot{a} = U_w$ is also included in Fig. 2.6,
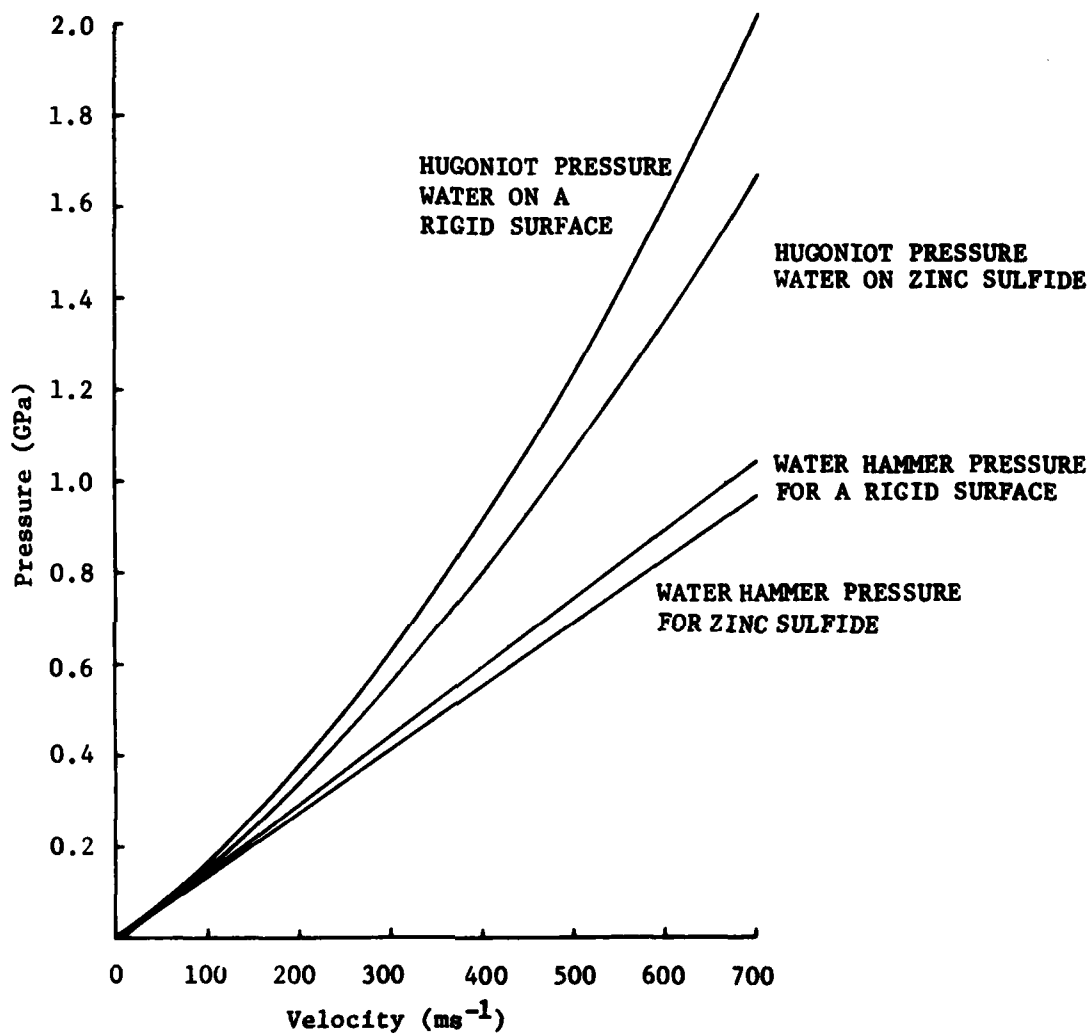
Figure 2.5. Hugoniot and water hammer pressures as a function of impact velocity for a rigid surface and zinc sulfide.

14

Contact radius a in μm, Elapsed time t in ns.

$a(\dot{a}=C_w)$

$a(\dot{a}=C_s)$

$a(\dot{a}=U_w)$

$a(\dot{a}=C_\ell)$

$t(\dot{a}=C_w)$

$t(\dot{a}=C_s)$

$t(\dot{a}=C_\ell)$

$t(\dot{a}=U_w)$

Velocity (ms^{-1})
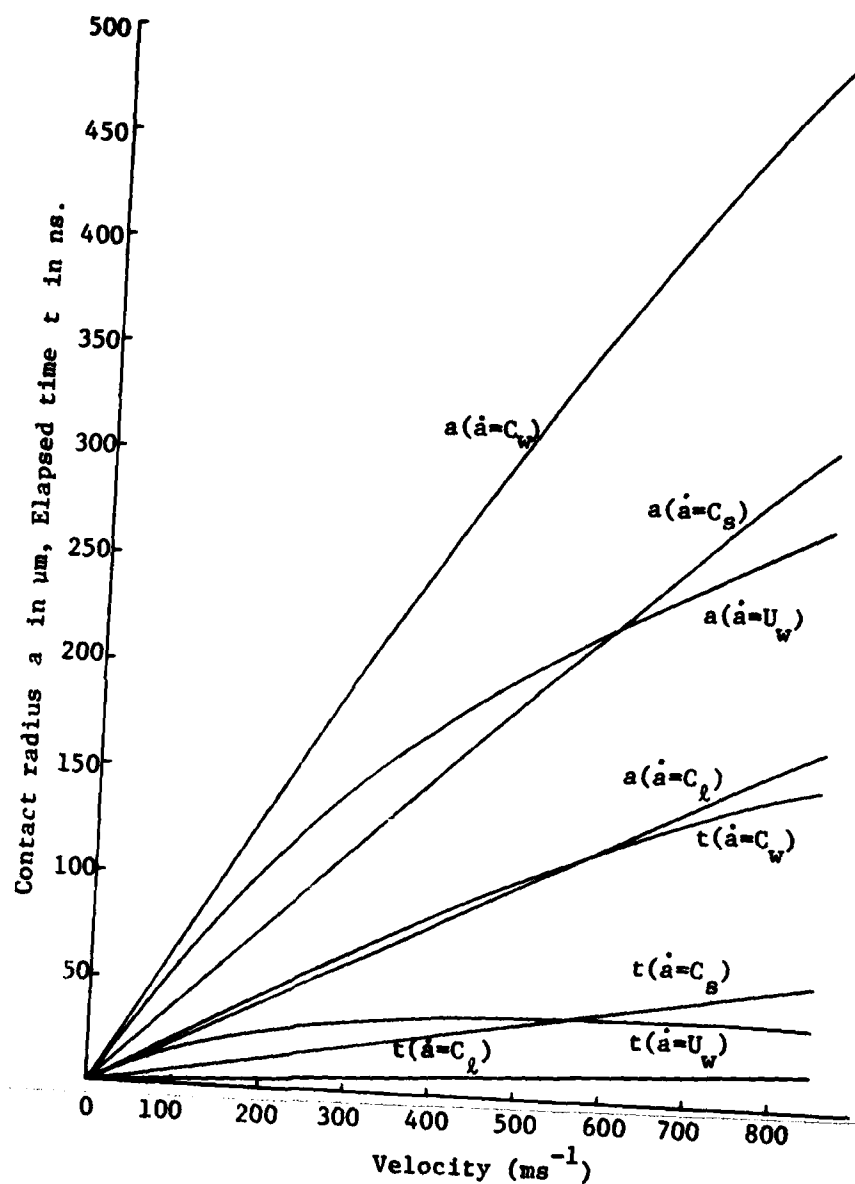
Figure 2.6. Calculated contact radii and elapsed times for stress wave separation from the contact zone and maximum in the peak pressure distribution.

15

since it was previously shown to correlate the experimental measurements of the central undamaged zone for water drop impacts on polymethylmethacrylate (Adler and James, 1979).

2.3   TRANSIENT STRESSES

The form of the pressure distribution suggested by the previous re-examination of the available data is completely compatible with the form of the pressure loading used in an analytic solution developed by Blowers (1969) to evaluate the stresses in an elastic half-space. The computational scheme used to evaluate the analytic solution offers the advantages of being economical to run on a digital computer and the stresses are not dependent on the computational grid dimensions. The disadvantage of the analytic approach originally formulated by Blowers is that it is only applicable up to the time at which lateral outflow initiates when the magnitude of the pressure is usually assumed to decrease precipitously. However, according to the results in Fig. 2.4 the above restriction may be relaxed somewhat. A new solution for evaluating the stresses in an elastic body due to an arbitrary pressure distribution has been derived by Adler, Botke, and James (1979).

The principal tensile stresses were determined using Blowers' solution for the same impact conditions considered by Rosenblatt and co-workers for a 2 mm water drop impacting a zinc sulfide target at 222 ms^{-1} (Rosenblatt, et al., 1977). The comparison between the results from the analytical solution and the limited results published for the finite difference computations was excellent. It is therefore concluded that Blowers' analytical solution adequately describes the transient stress states in the target material during the pressure build-up stage of the surface loading. The similarity in the computed values for the analytical and numerical schemes also lends support to our conjecture that the pressure spike at the periphery of the expanding contact zone may be of secondary importance with regard to the transient stresses in the target.

16

The condition $\dot{a} = C_w$ determines the maximum radial extent of the contact zone and the time after initial contact for which Blowers' solution would be applicable in accordance with the discussion in Section 2.2. It is seen from Fig. 2.6 that the time over which Blowers' solution is applicable is 44 ns for an impact velocity of 200 ms^{-1} and 120 ns when the impact velocity is 600 ms^{-1}. The calculated radial stress components 5 μm below the surface of the zinc sulfide target generated by a 2 mm water drop impacting at 200 and 600 ms^{-1} are shown in Fig. 2.7 and 2.8. At 44 ns (impact at 200 ms^{-1}) the shear wave front would have reached a radial distance of 0.155 mm. This corresponds to the first peak in the radial stress distribution at 45 ns in Fig. 2.7. The shear wave at 120 ns for the 600 ms^{-1} impact would have reached a radial distance of 0.427 mm consistent with the stress distributions in Fig. 2.8. The radial locations at which the shear wave separates from the contact zone are indicated in Fig. 2.7 and 2.8.

From the temporal evolution of the radial stress components it is seen that tensile stresses develop before the shear wave separates from the contact zone. After shear wave separation a second peak develops in the radial stress distribution corresponding to the propagation of the shear wave: its initiation can be seen in Fig. 2.8 for t=45ns . The forward peak, whose location corresponds to the shear wave front, rapidly becomes dominant. However for longer times the magnitude of the initial peak is the location of the maximum tensile stress. The location of this peak corresponds to the radial location of the Rayleigh wave which would be formed just after the shear wave. The character of the fractures shown in Fig. 2.2a may therefore be related to the calculated changes in the form of the stress wave structure and the associated transient stress and displacement fields in the target.

The initial development of significant radial tensile stresses in the vicinity of the surface of the specimen is responsible for the onset of the circumferential fractures which delineate the boundary of the

17
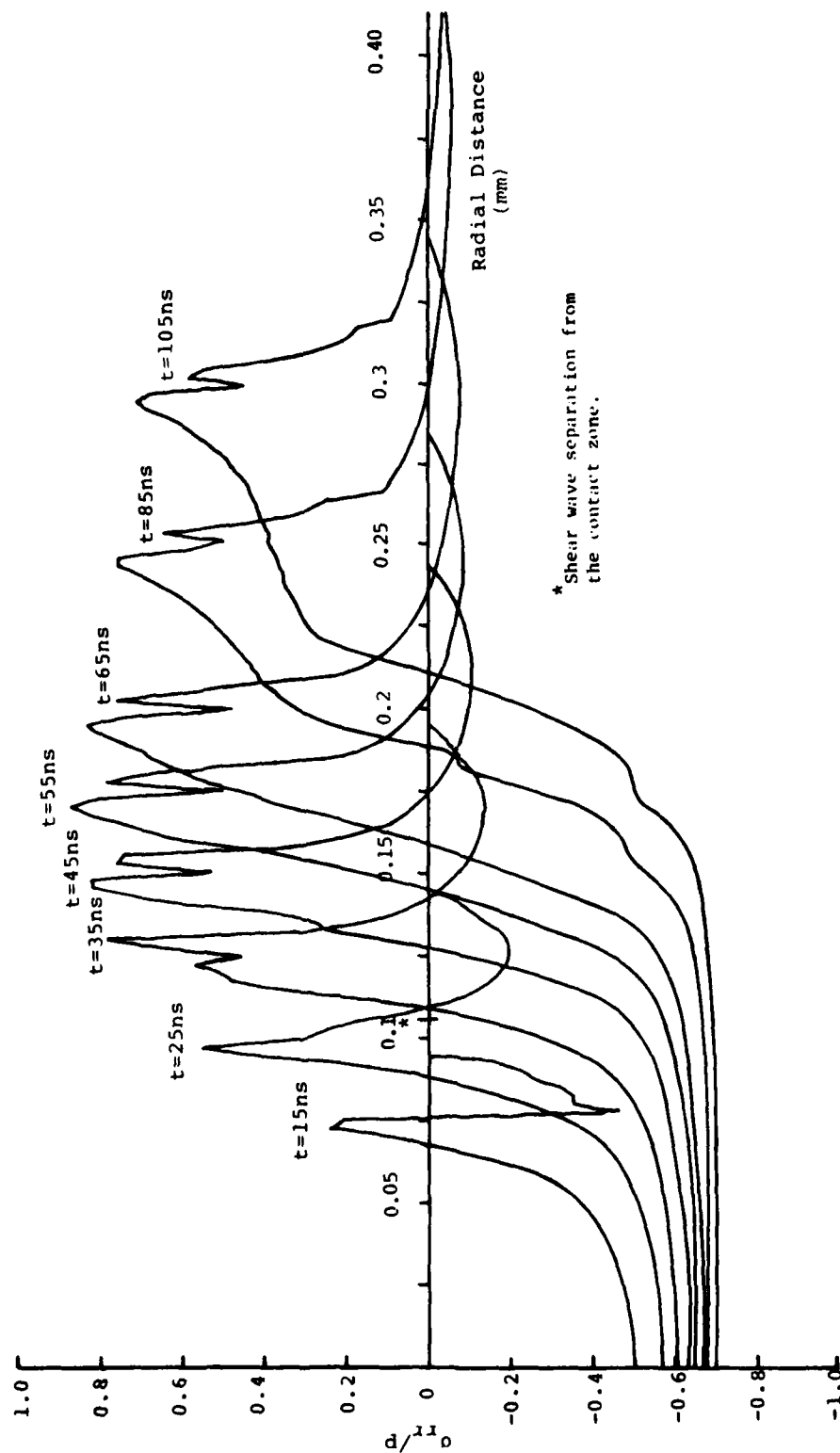
Figure 2.7. Temporal development of the normalized radial stress component for a 2 mm water drop impacting a zinc sulfide target at 200 ms^{-1}.

18

Radial Distance (mm)

0.55   0.50   0.45   0.40   0.35   0.30   0.25   0.20   0.15   0.10

T=105ns

T=65ns

T=45ns

*Shear wave separation
from the contact zone.

T=25ns

1.6 1.4 1.2 1.0 0.8 0.6 0.4 0. -0. -0.4 -0.6 -0.8 -1.0

σ_{11}/p
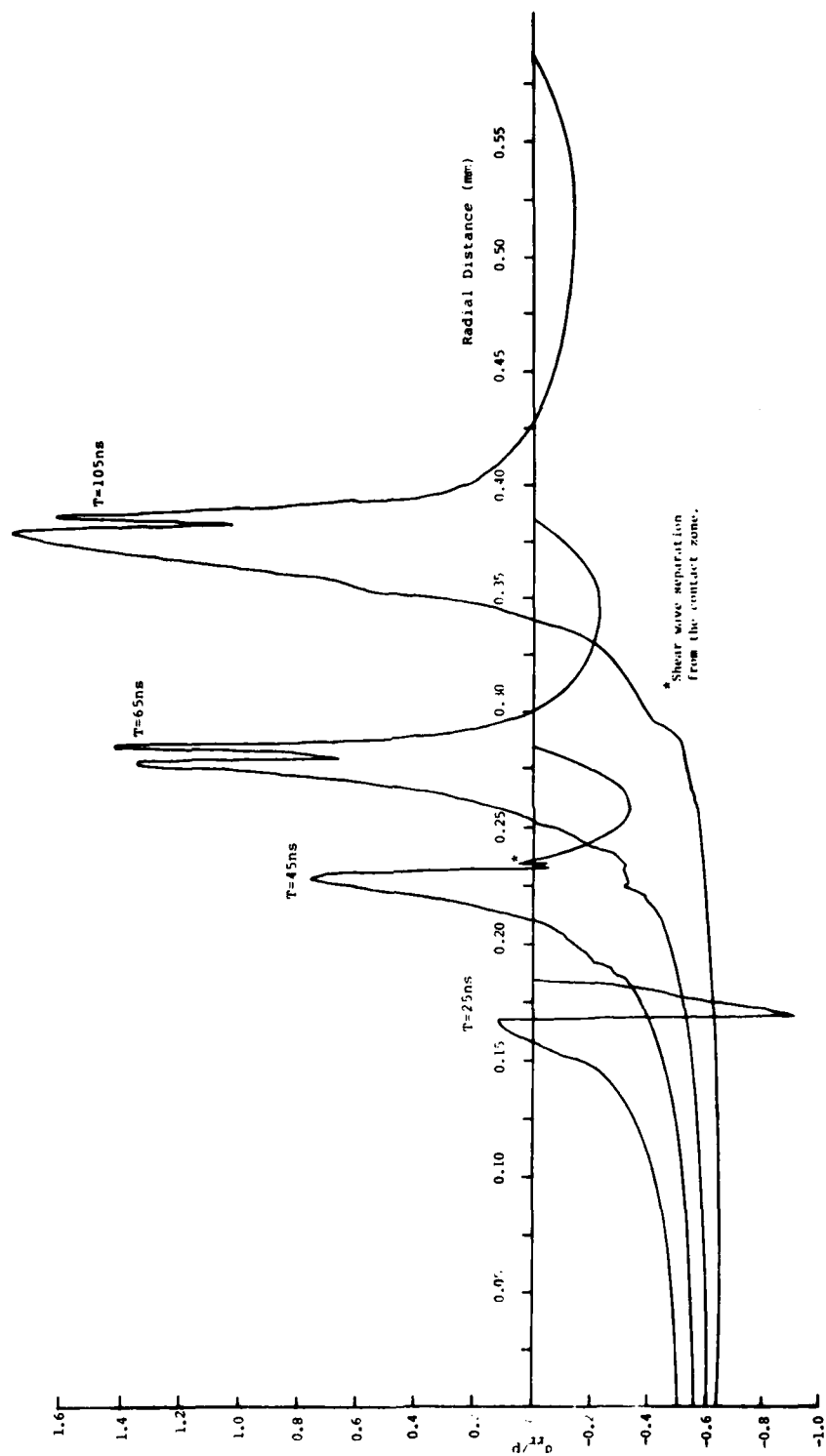
Figure 2.8. Temporal development of the normalized radial stress component
for a 2 mm water drop impacting a zinc sulfide target at 600 ms^{-1}.

19

central undamaged zone. It is our conjecture that the Type I fractures identified in Fig. 2.2a are due to the stress states associated primarily with the development of the shear wave both prior to and after its separation from the contact zone. The monotonic increase in the fracture depth corresponds to the increase in the magnitude of the tensile stress with radial distance. The subsequent formation of the Rayleigh wave is responsible for the Type II fractures. As is well known the influence of the Rayleigh wave decreases exponentially with depth, so the fracture trajectory of the Type II fractures tends to conform to the shape of the Type I fractures with increasing depth where the stresses associated with shear wave may replace the Rayleigh stresses. At larger radial distances the Rayleigh stress are dominant. Shallow fractures normal to the surface are formed. The generation of intermediate to far field fractures by Rayleigh waves is consistent with the experimental observations of Bowden and Field (1964) for glass. The sorting out of the stresses responsible for the near-field fractures is a new interpretation of the transient stress conditions.

The above comparisons indicate how Blowers' solution can be used to considerable advantage in acquiring an understanding of the transient stresses which develop in the target material economically, since it offers fine resolution for the stresses generated prior to fracture initiation. Insights into the potential fracture response can be acquired, even though once fracture initiation takes place finite difference computations may be required. The finite difference computational procedures provide a viable approach if the computational grid can accommodate the finer details of the subsurface fracture trajectories shown in Fig. 2.2a.

20

3.0 EXPERIMENTAL OBSERVATIONS

The characteristic features of water drop impact damage in an essentially elastic, homogeneous, and isotropic material (zinc sulfide) were described in Section 2. Several conjectures were made with regard to the damage process and the probable causes for the observed fracture patterns. Quantitative measurements of the reasonably identifiable features of the water drop impact damage in zinc sulfide have been made and will be summarized in Section 3.1. These measurements are over an extended velocity range and several features not considered in Section 2 are observed when the impact velocity exceeds 500 ms^{-1}. A tendency for radial fracturing, the development of fractures below the impact site parallel to the target's surface, and the initiation of material ejection are evident at the higher impact velocities.

The quality of the spherical water drop impact experiments and the range of impact conditions presently available in the ETI liquid drop impact facility provide an excellent data base for comparing simulations of actual water drop impacts. Experiments using well-characterized water jets and nylon bead collisions were undertaken for this purpose. A series of water jet impacted specimens representing nominal 2 mm water drop impacts from 300 to 600 ms^{-1} were received from the Cavendish Laboratory. The form of the damage for equivalent impact conditions is compared with spherical water drop collisions and some significant differences in the qualitative and quantitative features of the impact damage are found to exist. These findings are summarized in Section 3.2. The nature of the damage produced by nylon bead impacts on zinc sulfide is investigated in Section 3.3. The general character of the damage is found to be quite similar to a water drop collision, but the selection of equivalent impact conditions is not straightforward. However the potential for producing similar impact damage is shown to be quite high.

21

The water drop impact damage in polycrystalline calcium fluoride
is examined in Section 3.4. The polycrystalline fracture behavior is
related to our prior observations of single crystal response (Adler and
James, 1979).

3.1 WATER DROP IMPACTS ON ZINC SULFIDE

A discussion of the grain structure in CVD zinc sulfide can be
found in Adler, Botke, and James (1979). The columnar grain dimensions
for the material used throughout this investigation of zinc sulfide are
given in Table 2.1 along with other relevant properties for this material.
Specimens were prepared so that the impact face was perpendicular to the
growth direction. Measurements will be provided for the parameters iden-
tified in Section 2 to quantify the impact damage. These include the
radial distance corresponding to the onset of the circumferential frac-
tures which delineate the extent of the central undamaged zone, the
radial location of the depressed annulus assumed to correspond to the
maximum in the peak pressure and the initiation of lateral outflow, and
the radial locations and depths of the dominant Type I and Type II frac-
tures due to spherical water drop collisions on CVD zinc sulfide.

Measurements of the radius of the central undamaged zone were
taken from transmitted light micrographs of the impact face of the speci-
mens at a magnification of 100X. There was a notable difference between
the radii for etched and unetched surfaces as shown by the comparison pre-
sented in Fig. 2.1a and b. The readings reported are for surfaces etched
with hydrochloric acid. There is some uncertainty in defining the bound-
ary of the central undamaged zone due to the variation in identifying the
shallow fractures comprising the transition region surrounding the cen-
tral zone on the micrographs. The observed variance is recorded in
Table 3.1.

Table 3.1. Experimental Measurements of Water Drop Impact Damage Parameters for Zinc Sulfide.

Shot No.	v_o (m s^{-1})	$2r_o$ (mm)	FRACTURE INITIATION		PEAK PRESSURE MAXIMUM		TYPE I FRACTURES		TYPE II FRACTURES	
			$2a_c$ (mm)	a_c/r_o	$2c$ (mm)	c/r_o	Location (mm)	Depth (mm)	Location (mm)	Depth (mm)
1251	240	2.09-2.20	0.21-.22	0.096-.105			0.197	0.056		
1204	317	2.30-2.38	0.28-.29	0.118-.126			0.25	0.10	0.34	0.11
1197	317	2.22-2.25	0.26	0.115-.119			0.263	0.097	0.355	0.11
1198	317	2.25-2.32	0.26-.27	0.112-.123						
1200	354	2.22-2.30	0.31	0.135-.142			0.353	0.233	0.43	0.245
1040	400	2.14	0.28-.30	0.131-.150			0.26	0.16	0.58	0.223
1237	405	2.10	0.31-.32	0.148-.155	0.529	0.252-.256	0.34	0.245	0.50	0.235
1221	405	2.19-2.35	0.35-.36	0.149-.165			0.368	0.253	0.55	0.422
1245	498	2.29	0.37-.38	0.161-.171	0.665	0.290-.300	0.387	0.453	0.593	0.51
1235	540	2.30	0.43-.45	0.187-.197	0.686	0.300	0.368	0.440	0.733	0.653
1247	562	2.22-2.24	0.42-.45	0.188-.204	0.724-.782	0.324-.356	0.459	0.68	1.065	0.688
1249	582	2.22-2.29	0.40-.43	0.175-.202	0.786	0.344-.370	0.390	0.720	1.08	0.64
1231	650	2.21-2.39	0.40-.45	0.168-.204	0.761-.812	0.318-.369	0.570	0.960	1.125	0.90
1255	710	2.04-2.13	0.48-.50	0.225-.245	0.838	0.394-.410	0.556	1.33	1.685	0.852
1250	775	2.10 est.	0.50-.56	0.238-.267			0.444	1.815	2.24	1.28
1254	825	2.05-2.09	0.57-.60	0.273-.293			0.48	2.4	2.0	1.63

The general form of the relations in Eq.(2.8) for the location of the contact radius (when various conditions are imposed on the rate of expansion) exhibits a linear variation with the drop diameter. The plots of the data will therefore be normalized with respect to the drop diameter.

The water drops generated in the liquid drop impact facility fall from a hypodermic needle into the path of the sabot mounted specimen. The falling drop is photographed for each test just prior to impact. Minor variations in drop size are evident using this system. The level of uncertainty in the drop radius in the current photographic system, the drop magnification, and general graininess of the high speed Polaroid film used for these records is taken into account in the tabulations in Table 3.1. The drop radius is a critical parameter in any data reduction procedure and fairly accurate determinations should be available. In view of its significance and that of the drop impact velocity, the photographic procedures used for these measurements are currently being improved in the ETI liquid drop impact facility. The maximum variation in the drop diameter is therefore also indicated in Table 3.1. The normalized radius of the contact zone, a_c/r_o , is given as a range of values which accounts for the experimental error introduced into the measurements of the actual drop radius and the radius of the central undamaged zone.

The next significant parameter which can be measured is the radius of the center of the depressed annulus. This measurement, the diameter 2c, is taken from profilometer traces through the center of the impact site. As seen in Fig. 2.2 there is some degree of arbitrariness in selecting the base of the depressed annulus; this is reflected by a range of values in Table 3.1.

On the basis of the analysis presented in Section 2, the normalized radii of the central undamaged zone, a_c/r_o , and the radial location of the maximum depth of the depressed annulus, c/r_o , are associated with the separation of the shear wave from the contact zone and the maximum in the peak pressure, respectively. These measurements are plotted in Fig. 3.1 and compared with the predictions made in Section 2. The
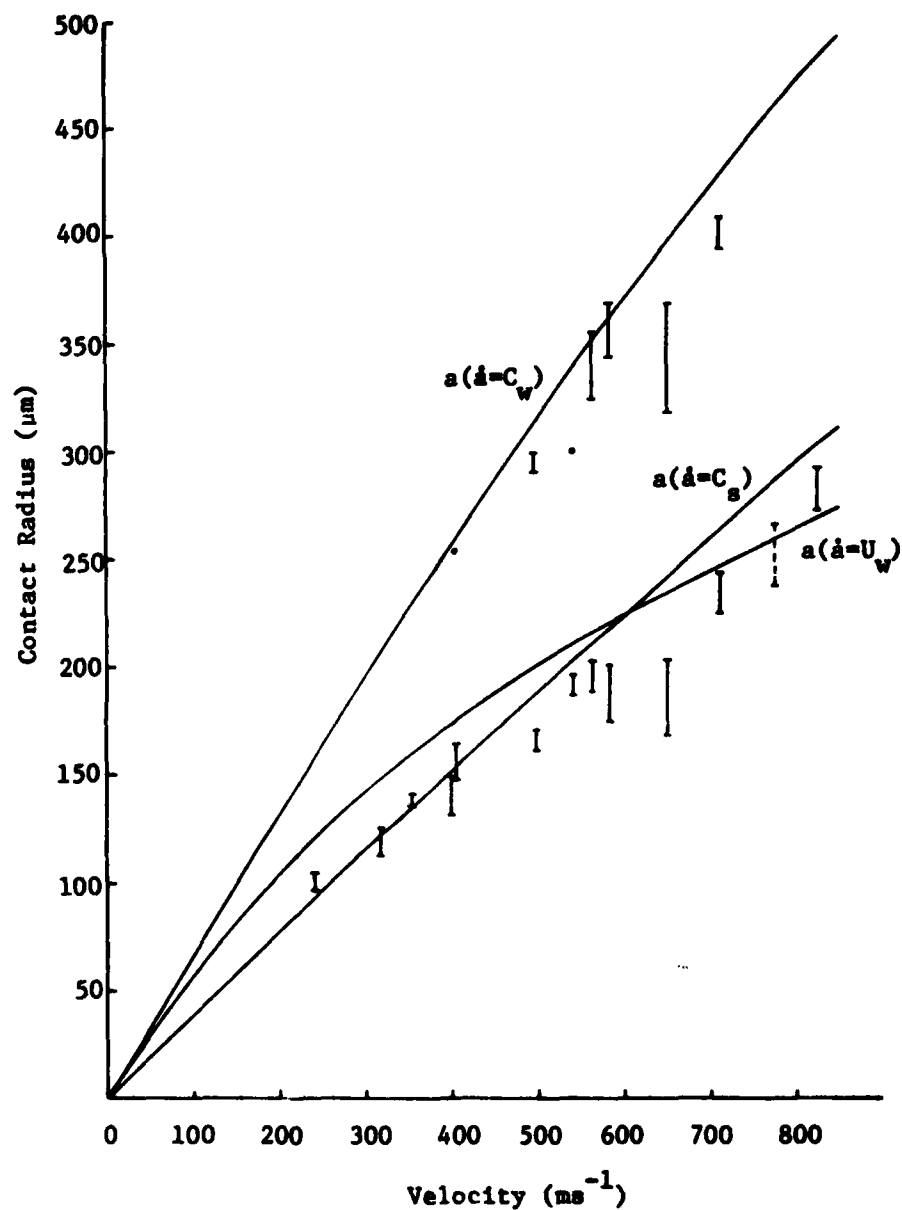
24

Figure 3.1. Measured values for the onset of circumferential
fractures, a_c/r_o , corresponding to separation
of the shear wave from the contact zone and the
maximum in the peak pressure, c/r_o , corresponding
to the condition $\dot{a}=C_w$.

experimental data shows a favorable correspondence with the analytical relations. The relation $\dot{a} = U_w$ is also plotted in Fig. 3.1, since this was proposed previously as the criterion for lateral outflow jetting in polymethylmethacrylate (Adler and James, 1979). In view of the correlation established for zinc sulfide this result is subject to revision.

A number of specimens were sectioned in order to observe the subsurface fracture patterns. Since only one thin section can be obtained from each specimen, a subjective determination had to be made regarding the diameter selected. The major criterion used was that the influence of the larger surface polishing scratches be minimized. A satisfactory polishing procedure for these specimens was developed during the course of the past year's effort, since the quality of the surface has to be quite high in order to minimize scratch interactions with the stresses imposed by the water drop collision. The majority of the specimens were polished by a commercial polisher, but for the most part these proved to be marginally acceptable. The fractures due to the larger surface scratches are quite deep and of greater circumferential extent compared to the fractures originating at small surface flaws. They are readily identified. The sections were therefore selected which passed through regions essentially devoid of the larger surface scratches.

As indicated in Section 2, two forms of fracture trajectories were observed on the thin sections. They are referred to as Type I and Type II fractures as shown in Fig. 2.2a. The radial distance from the impact center and the depth measured normal to the surface of the specimen are two parameters selected to characterize these fractures. The location of these fractures is determined in part by the distribution of surface flaws, but once the obvious larger surface scratches were eliminated the annulus in which these flaws originated was found to be of narrow radial extent. The depth of the fractures was quite consistent as could be observed with an optical microscope by focusing through the impact damage.

26

Two radial locations and fracture depths were measured for each fracture type due to the symmetry of the impact as seen on the thin sections. In some cases fracture doublets were found: two closely spaced fractures of the same type without a clear distinction as to which one could be considered the dominant fracture. The average values of the fracture locations and depths, including fracture doublets are listed in Table 3.1.

The average fracture dimensions are plotted as a function of the impact velocity in Fig. 3.2 to 3.4 without any provision for the variation in drop diameter since this would require the introduction of an assumption as to how these fracture parameters vary with drop diameter which is not known at present. The form of the data is most interesting and for the most part reliable. A uniform variation in the radial location of the Type I and Type II fractures is seen up to slightly beyond 500 ms^{-1}. A transition is noted in the location of the Type II fractures in the vicinity of 550 ms^{-1}. Slightly above this impact velocity random radial fractures are beginning to appear possibly indicating a change in the damage mode.

Overviews of these radial fractures are shown for shot no. 1231 and 1250 in Fig. 3.5. A detail of the longer radial fractures seen on shot no. 1250 and the form of the radial fractures in the interior of the target for shot no. 1255 are shown in Fig. 3.6. It is observed that the radial fractures originate on a fairly random basis at sites branching from the circumferential fractures. Specification of the mechanism for initiation and propagation of the radial fractures requires further study.

The series of mean surface profiles in Fig. 3.7 shows the variation in the general form of the surface profiles as well as the tendency for ejection of the central portion of the damaged material due to the intensity of the elastic recovery which would be experienced at the higher impact velocities. The profiles for the impacts at 775 and 825 ms^{-1}

27
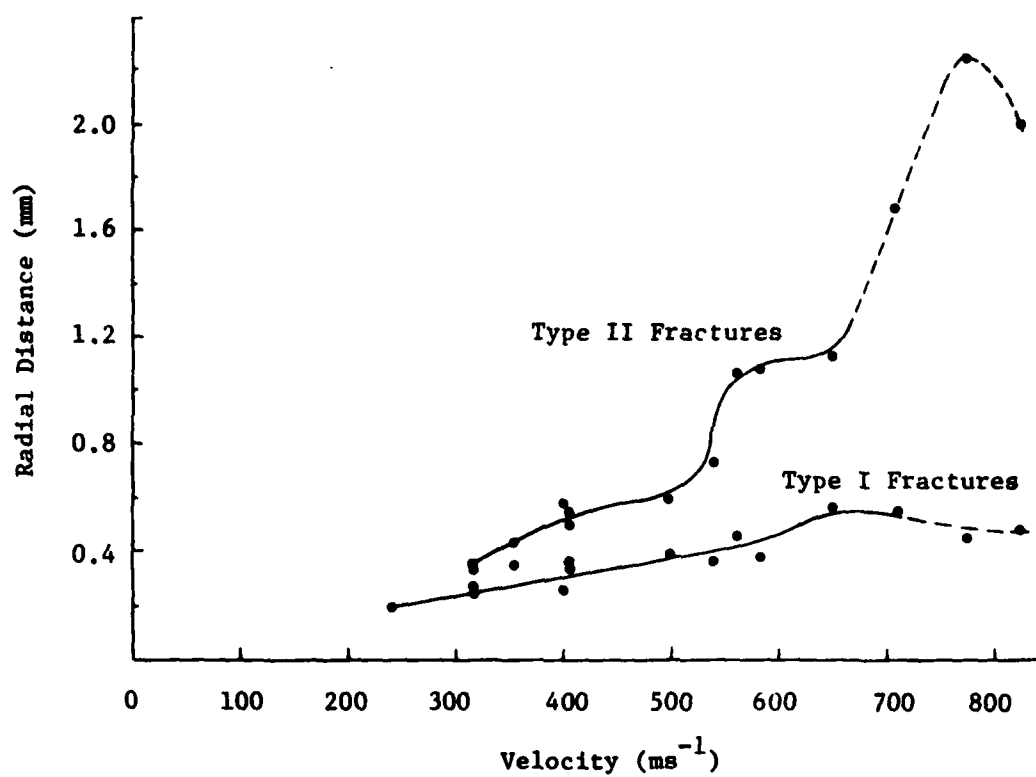
Figure 3.2. Radial distance to dominant Type I and Type II
fractures as a function of impact velocity for
water drop impacts on zinc sulfide.
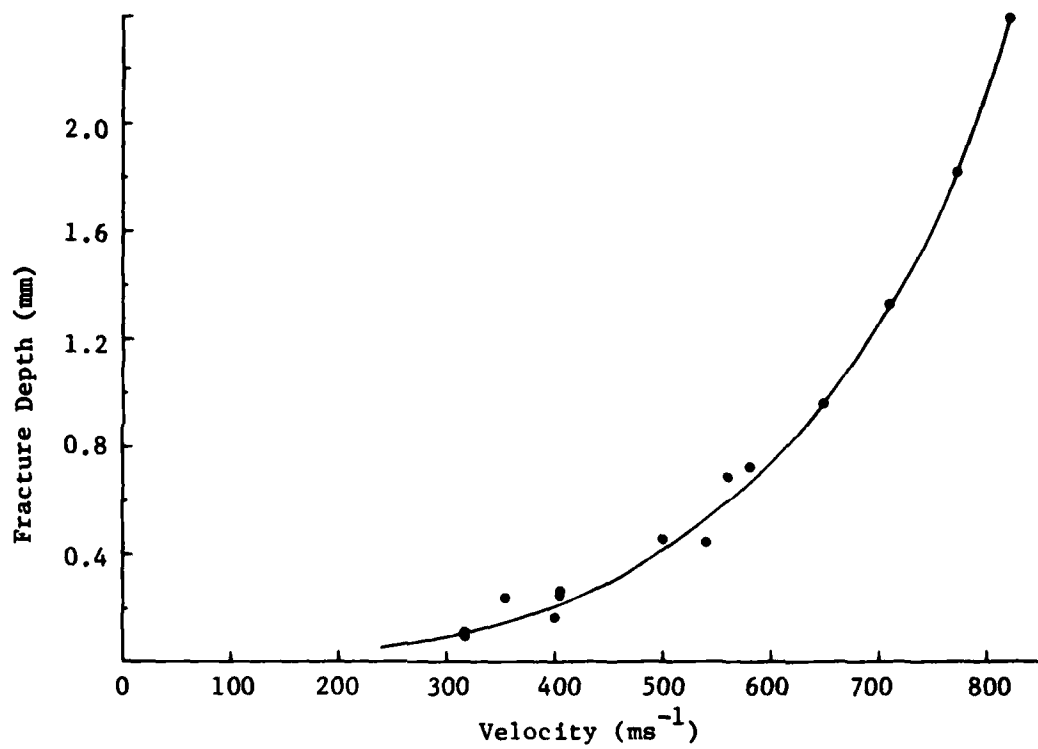
Figure 3.3. Penetration depth for Type I fractures
as a function of impact velocity for
water drop impacts on zinc sulfide.

29
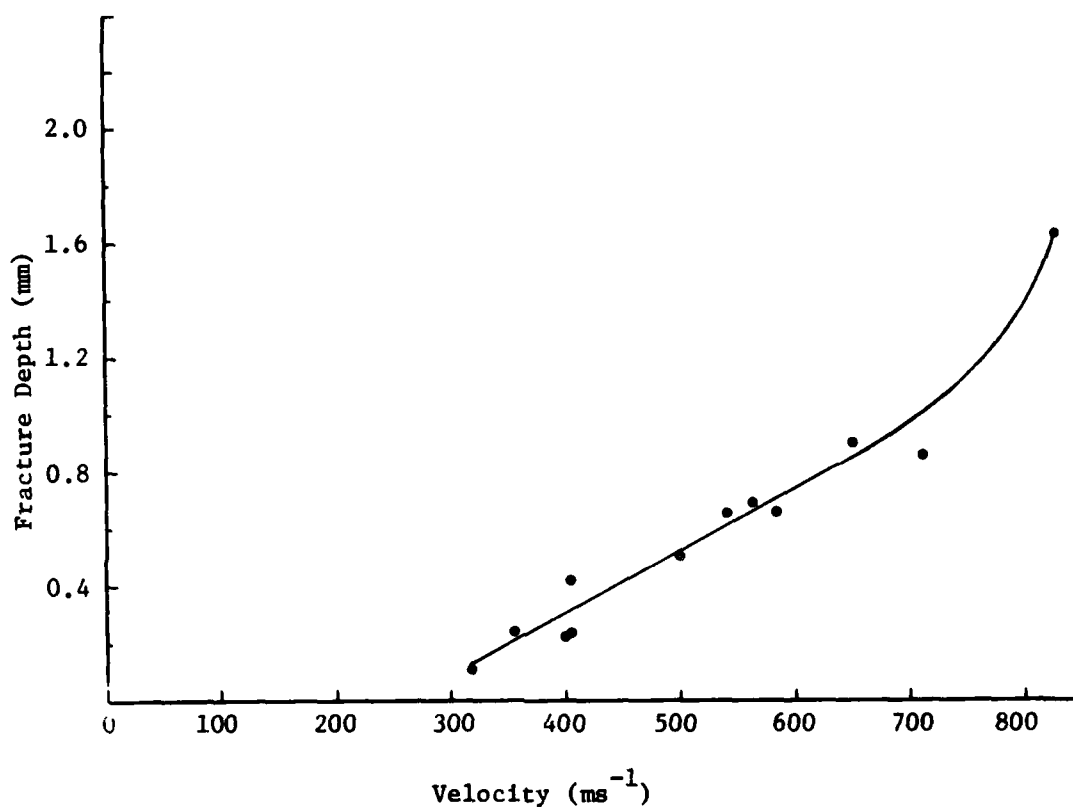
Figure 3.4. Penetration depth for Type II fractures as a
function of impact velocity for water drop
impacts on zinc sulfide.

(a) Shot no. 1231: 650 ms^{-1}.

(b) Shot no. 1250: 775 ms^{-1}.

Figure 3.5. Overview of radial fractures seen on zinc sulfide specimens at impact velocities beyond 550 ms^{-1}. Transmitted light illumination.

(a) Detail of origin of longer radial fractures
    shown in Fig. 3.5b.

(b) Radial fractures seen in cross section for Shot no. 1255.
    Note also detail of the horizontal fracture below the
    impact site. The deep fractures running nearly parallel
    to the surface of the specimen are believed to be anomalous.

Figure 3.6. Detail of radial fractures.

Figure 3.7. Surface profiles for water drop impacts on zinc sulfide for a range of impact velocities.
(a) Shot no. 1245: 498 ms^{-1}; (b) Shot no. 1235: 540 ms^{-1};
(c) Shot no. 1249: 582 ms^{-1}; (d) Shot no. 1231: 650 ms^{-1};
(e) Shot no. 1255: 710 ms^{-1}.

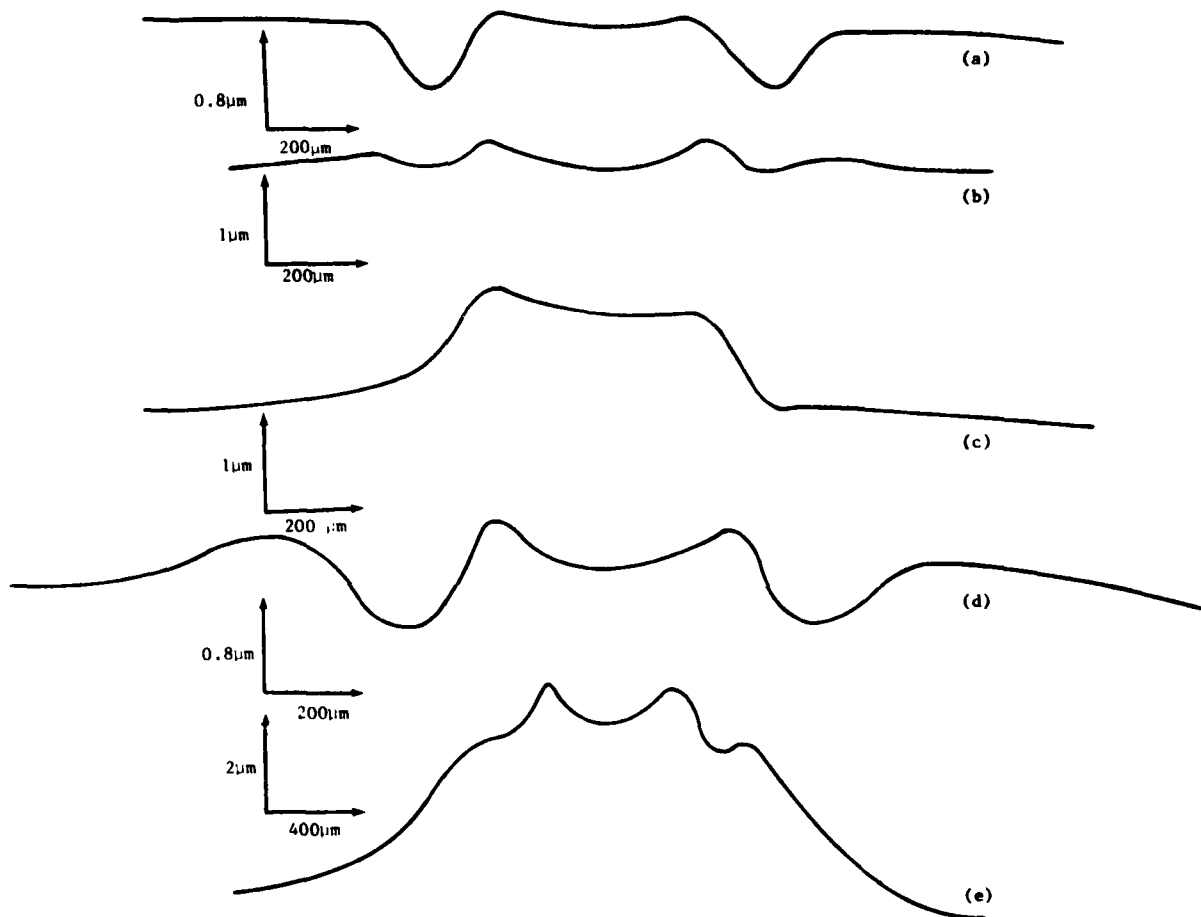(shot no. 1250 and 1254 in Table 3.1) appear as relatively featureless mounds of material elevated beyond the original plane of the impact face. The larger vertical displacements of the central damage annulus are accompanied by a single or bifurcated horizontal fracture plane below the impact site. The horizontal fracture first appears in shot no. 1249 at an impact velocity of 582 ms^{-1}. Cross sections of the higher velocity impacts are shown in Fig. 3.8. The origin of the deep horizontal fractures on the right hand side of Fig. 3.8a is not known; the specimens were thick enough to eliminate the influence of significant stress wave reflections from the back face of the specimen which may interact with the water drop impact damage. The extended fracture on the left hand side of Fig. 3.8c is due to the preparation of the thin section. The horizontal fractures are presumed to be due to the elastic recovery of the central depressed zone which would become more intense at the higher impact velocities. Finally the SEM micrograph in Fig. 3.9 shows an uplifting of fractured material around about one-third of the impact site (the lighter band just outside the central undamaged zone). Further increases in impact velocity should result in the onset of cratering as the central portion of the impact damage is ejected from the specimen's surface.

The transition in the mode of damage beyond 500 ms^{-1} described above does not appear to have a disruptive influence on the fracture depths as seen from Fig. 3.3 and 3.4. The fracture depths increase uniformly as v_o^n. For Type I $3.0 \leq n < 3.4$ fits the data quite well over the complete velocity range, whereas $n=1$ fits the fracture depth data for the Type II fractures except for the velocities in excess of 700 ms^{-1}. At the higher impact velocities there is a tendency for the Type I fracture depths to become predominant as seen in the cross sections in Fig. 3.8. The magnitude of the rapid increase in the radial location of the dominant Type II fractures at 550 ms^{-1} and above in Fig. 3.2 requires further investigation.

(a) Shot no. 1255.
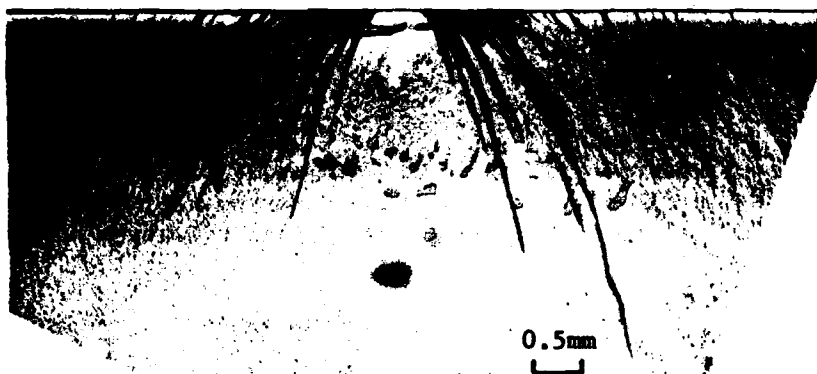
(b) Shot no. 1250.
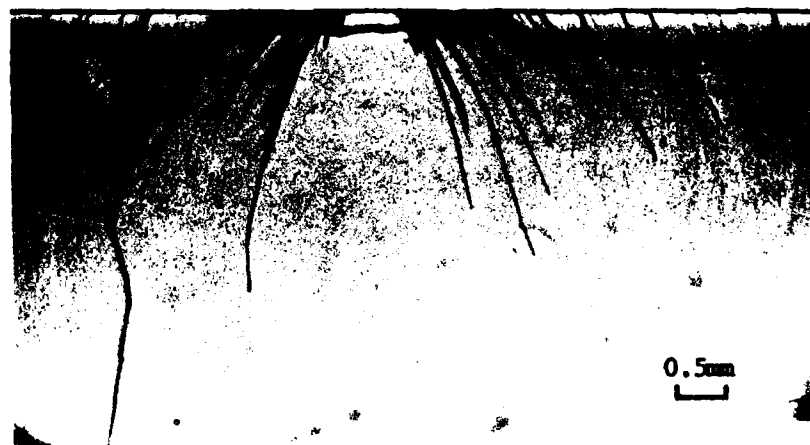
(c) Shot no. 1254.

Figure 3.8.   Cross sections of higher velocity water drop
impacts on zinc sulfide. Note presence of
horizontal fracture below impact site for the
more severe impact conditions.

35

400 μm
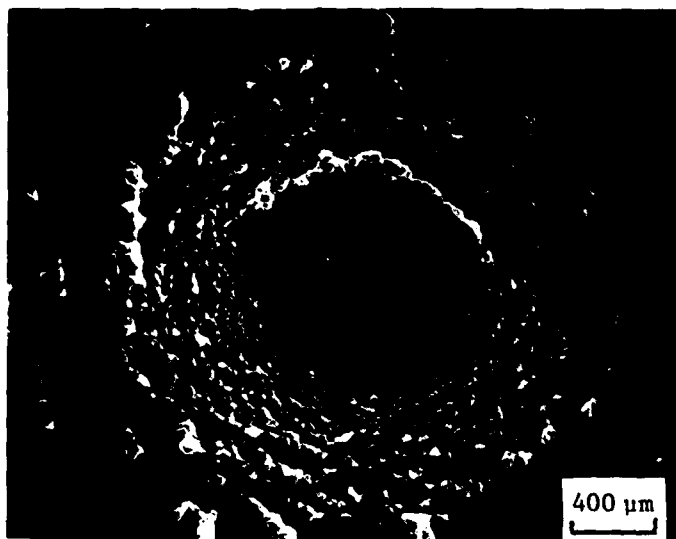
(a) SEM micrograph showing upraised region as a lighter band just outside the central undamaged zone.

200 μm
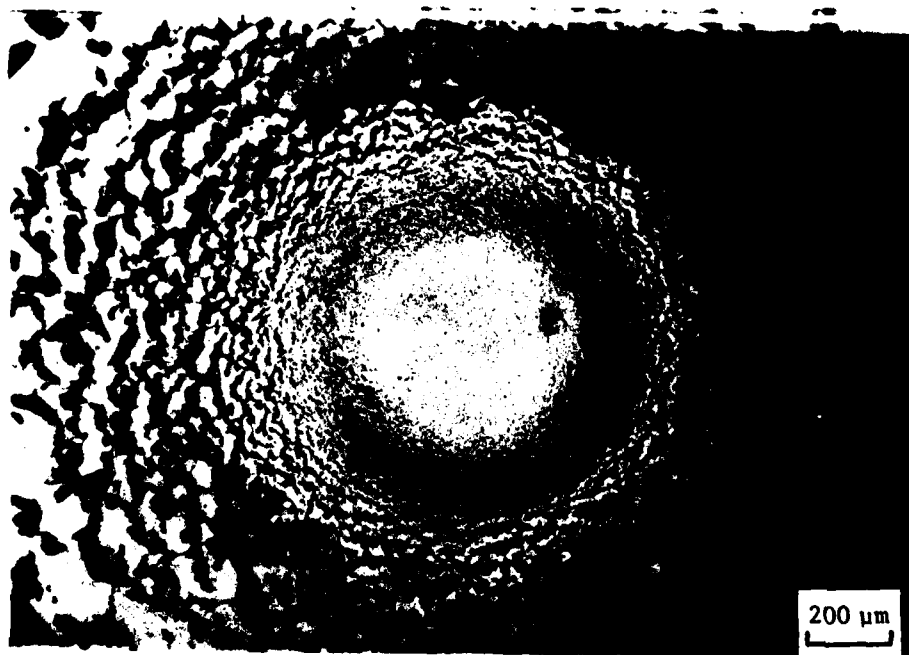
(b) Optical micrograph showing same region as dark shadow.

Figure 3.9.   Potential ejection of material from the surface for water drop impacts above 700 ms^{-1} as illustrated by shot no. 1250 at 775 ms^{-1}.

3.2   WATER JET IMPACTS ON ZINC SULFIDE

The water jet was developed at the University of Cambridge in the late fifties as a useful laboratory device for evaluating the effects of water impacts on materials. The correspondence between the loading imparted to a surface by a water jet and by a spherical drop was considered in the initial paper on this subject (Bowden and Brunton, 1961); the correspondence has been strengthened within the last few years (Field, et al., 1976; 1979). Empirical correlations are developed based on the size of the central undamaged zone produced primarily in polymethylmethacrylate specimens by water jets using various nozzle diameters and water drop impacts with varying diameters for velocities ranging from 200 to 400 ms^{-1}. These correlations are used to establish the equivalence relations between the water jet parameters and spherical drop collisions. Field and co-workers conclude that water jets with a standoff distance of 10 mm and nozzle diameters from 0.4 to 2.4 mm can simulate the effects of water drops ranging in size from 2 to more than 35 mm over a velocity range from 100 to 600 ms^{-1}. The effects of a 2 mm water drop collision can be simulated over a velocity range from 300 to 600 ms^{-1}.

It is hypothesized that the initial water hammer pressure for both cases controls the amount of damage. Thus damage extension during the period of lateral outflow is taken to be relatively small and not significantly different for a water drop and water jet over a velocity range from 100 to 600 ms^{-1}.

Kinslow (1974) also used a water jet as a simulation of water drop impacts at velocities ranging from 600 to 1500 ms^{-1}. This work was directed toward quantifying liquid impact damage on slip cast fused silica radomes in the supersonic impact regime. The craters produced by water drop impacts on radomes fired down a test track using a rocket sled and the craters produced by the water jet device in the laboratory provide

the basis for establishing equivalence relations. Again, the basis for comparison is in terms of the macroscopic features of the craters formed by both test conditions. It should be noted that the test conditions represented by the rocket sled are quite variable with respect to the drop velocity, diameter, and shape. The comparison with specific craters is therefore quite crude, since the conditions under which they were formed are not known. Kinslow (1974) further argued that a spherical drop passing through the shock wave ahead of a radome traveling at supersonic speeds is in essence a short jet due to the distortion of the drop during its transit through the shock layer. Thus a water jet may be a better representation for this flight condition. A sizable analytical effort relating to the impact conditions and materials investigation were also undertaken in conjunction with this experimental capability.

While the use of water jets has many advantages from a pragmatic point of view, additional work is required before a convincing comparison with water drop impact damage can be established. The single impact may show damage of a similar nature on a gross scale. This does not provide any indication of the similarities or differences in the type of subsurface damage which may develop which is very important to the progression of damage and eventual erosion in a multiple impact environment. The subtle aspects of the initial damage are certainly significant in the case of low-strength polycrystalline ceramics, whereby the useful optical quality can be degraded to unacceptable levels during exposure to a relatively small number of impacts in the vicinity of the initial collision (Adler and Hooker, 1976; Hackworth and Kocher, 1977). Furthermore, the water jet/water drop analogy deemphasizes the importance of lateral outflow and concentrates on direct pressure effects. The influence of lateral outflow effects due to a water jet and a drop for subsequent impacts has not been evaluated, however the possibility again exists for significant differences in the sequence to occur. The unique response characteristics of each material, or class of materials, may have to be considered on an individual basis.

A comparison between all aspects--qualitative and quantitative, macroscopic and microscopic--of the fracture response of CVD zinc sulfide has been undertaken for water jet impacts determined to be equivalent to spherical water drop *collisions* in accordance with the correspondence established at the University of Cambridge (Field, et al., 1976). It is often assumed for various materials that this is the case in the rain erosion literature, however no definitive comparisons in support of this contention have ever been made. The controlled and well-documented water *drop impacts* obtainable in the liquid drop impact facility at ETI and the careful characterization of the water jets produced at the Cavendish Laboratory afforded the opportunity to investigate the fracture damage for each of these conditions. An investigation of this issue was made possible with the cooperation of Dr. John E. Field at the Cavendish Laboratory (Cambridge, England).

Specimens were prepared from the same lot of CVD zinc sulfide and polished by a commercial polisher. The material is the same as that used in the impact experiments described in Section 3.1. Duplicate water jet impacts were requested for nominal 2 mm equivalent water drops at 300, 400, 500, and 600 ms^{-1}. The plots of the correlations (Field, et al., 1976) indicate the equivalent drop diameter is 2.2 mm at 300 ms^{-1}, 1.8 mm at 400 ms^{-1}, 1.7 mm at 500 ms^{-1}, and 2.3 mm at 600 ms^{-1}. It is our understanding that the jet head dimensions and velocities are not measured for each impact but are determined from prior calibration of the water jet impact device. The magnitude of the variation possible in the formation of the jet and its impact velocity is not stated.

The same damage characterization procedures carried out for the water drop impacts were also carried out for the water jet impacts on zinc sulfide. Overviews of the impact damage for the specimens impacted at 300 and 600 ms^{-1} are shown in Fig. 3.10 and 3.11 along with comparable water drop impacts. The radial extent and concentration of the circumferential fractures seen in reflected illumination are noticeably greater

39
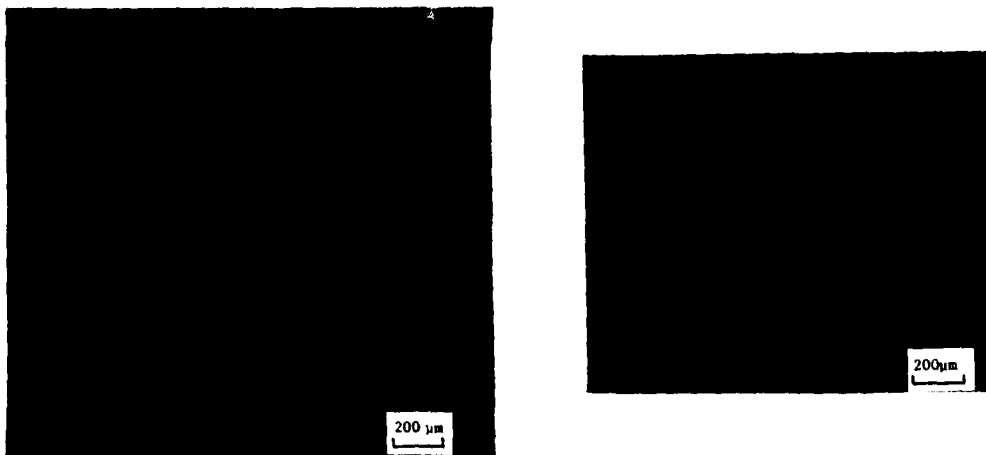
(a) Water jet impact in transmitted and reflected illumination.
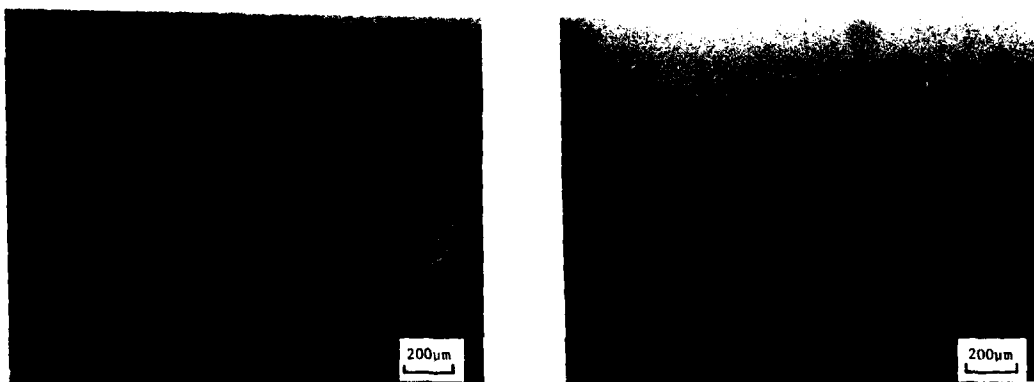
(b) Spherical water drop impact in transmitted and reflected illumination.

Figure 3.10. Comparison of water jet impacted specimen of zinc sulfide (equivalent 2 mm water drop impact at 300 ms^{-1}) with shot no. 1197 at an impact velocity of 317 ms^{-1}.
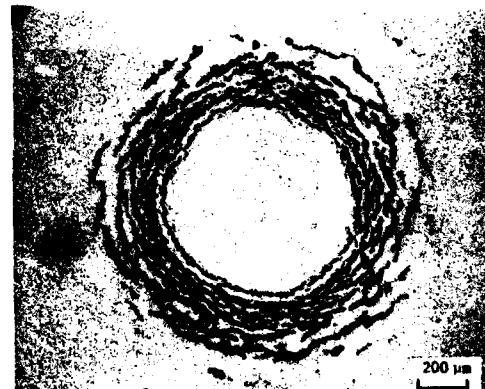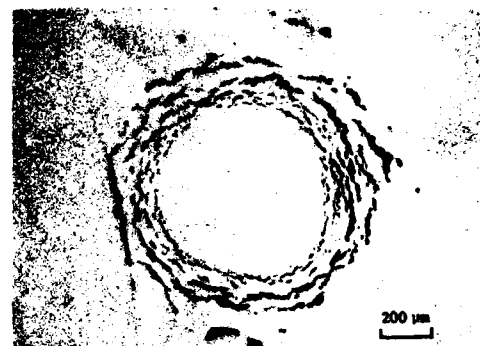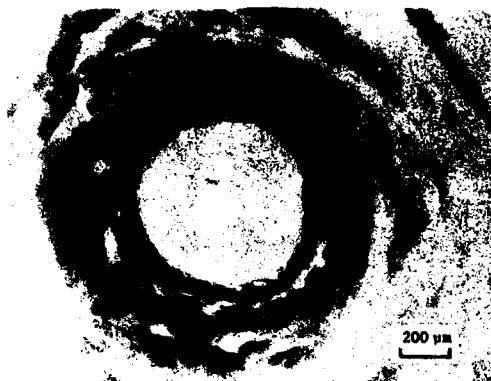
(a) Water jet impacts in transmitted and reflected illumination.

Figure 3.11. Comparison of water jet impacted zinc sulfide specimens (equivalent 2 mm water drop impact at 600 ms^{-1}) with shot no. 1249 at an impact velocity of 582 ms^{-1}. Note the difference in the extent and concentration of the damage. The micrographs for all three impacts are reproduced at the same magnication for direct comparison.
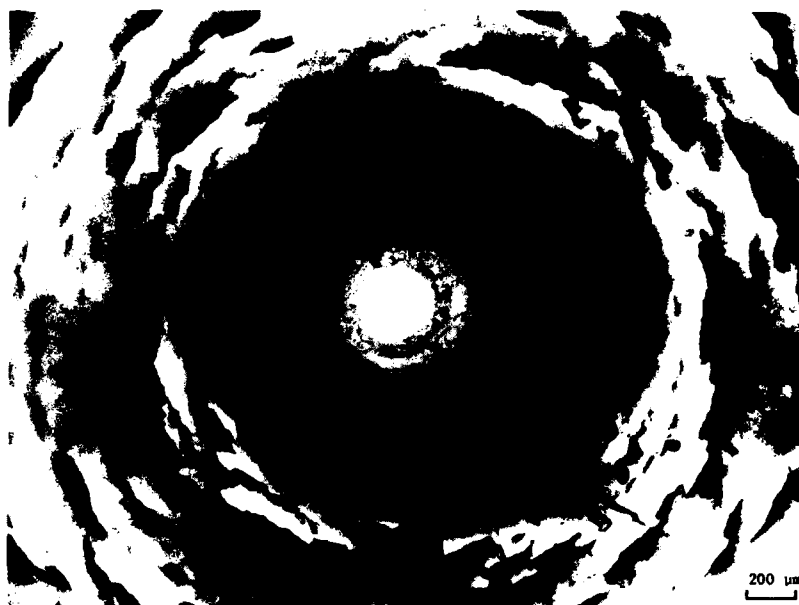
(b) Spherical water drop impact in transmitted and
    reflected illumination.

Figure 3.11. (continued)

for the water drop collisions. Another general observation is that there is a significant difference in the extent of the subsurface fractures when viewed in transmitted illumination. Furthermore, radial fractures are seen for water drop impacts at velocities below 600 ms^{-1}, however the water jet impacts at 600 ms^{-1} do not exhibit any evidence for the onset of radial fractures.

Surface polishing scratches were present on the impact face of the specimens which interacted with the impact damage, but their distribution was limited so that they did not exert a strong influence on the general fracture pattern. Only regions away from zones of significant scratch interactions were considered in this investigation.

Measurements of the central undamaged zone were made for the water jet impacts after etching the impact face with HCl. These measurements are tabulated in Table 3.2. These measurements indicate that the central undamaged zone is nearly twice the diameters found for spherical drop impacts and the variation in these diameters with impact velocity is considerably less than for water drop collisions. The surface profiles in Fig. 3.12 do not display the prominent depressed annulus found for water drop collisions and tend to produce much larger crack height differences for the circumferential fractures surrounding the central undamaged zone.

After the above measurements were taken the specimens were sectioned. A side-by-side comparison of the subsurface fracture patterns for water drop and equivalent water drop (water jet) impacted CVD zinc sulfide is shown in Fig. 3.13. The differences between the two forms of liquid impact become more drastic as the impact velocity increases. Type I fractures are generally dominant, and only a moderate semblance of Type II fractures is present on most impacts.

Table 3.2. Experimental Measurements of Water Jet Impact Damage Parameters for Zinc Sulfide.

Impact Velocity (ms⁻¹)	Equivalent Spherical Drop Diameter (mm)	Central Undamaged Zone Diameter (mm)	Type I Fracture				Type II Fracture			
			Left		Right		Left		Right	
			Location (mm)	Depth (mm)	Location (mm)	Depth (mm)	Location (mm)	Depth (mm)	Location (mm)	Depth (mm)
300	2.2	0.549	0.279	0.066	0.279	0.074	0.320	0.115	0.361	0.123
300	2.2	.569					—	—	.517	.271
400	1.8	.590	.410	.185	.410	.246	.714	.279	.689	.279
400	1.8		.394	.402	.394	.312	.681	.336	.722	.410
500	1.7	.569	.340	.361	.340	.369	.517	.353	.386	.246
500	1.7	.628	.328	.648	.397	.164	.476	.295	.492	.451
600	2.3	.637	.361	.131	.361	.574	.681	.418	.623	.328
600	2.3	.657	.397	.902	.377	.533				

44

Figure 3.12. Surface profiles for water jet impacted specimens of zinc sulfide.
(a) Equivalent 2 mm water drop impact at 400 ms^{-1};
(b) Equivalent 2 mm water drop impact at 600 ms^{-1}
corresponding to the two impacts shown in Fig. 3.11(a).

(a) Water jet impact equivalent to a 2 mm water drop
impact at 300 ms^{-1}.
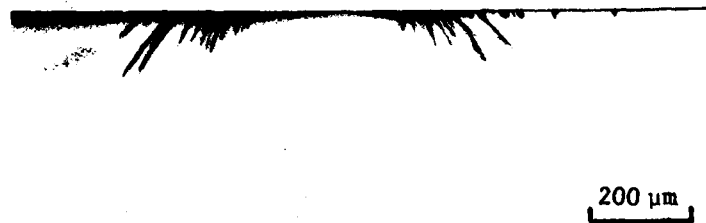
(b) Water drop shot no. 1204 at 317 ms^{-1}.

Figure 3.13.   Comparison of subsurface fractures due to water
jet impacts with spherical water drop impacts for
comparable impact conditions

0.5 mm

0.5 mm

(c) Water jet impacts equivalent to a 2 mm water drop impact at 400 ms^{-1}.

0.5 mm

(d) Water drop shot no. 1237 at 405 ms^{-1}.

Figure 3.13. (continued)

(e) Water jet impacts equivalent to a 2 mm water drop impact at 500 ms^{-1}.

(f) Water drop shot no. 1245 at 498 ms^{-1}.

Figure 3.13. (continued)

(g) Water jet impacts equivalent to a 2 mm water drop
    impact at 600 ms^{-1}.

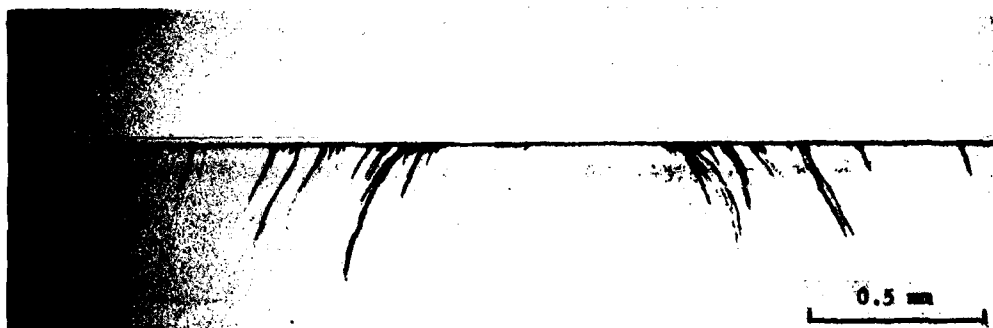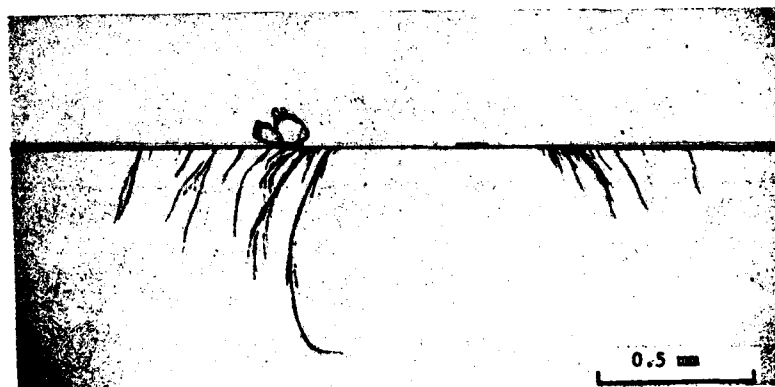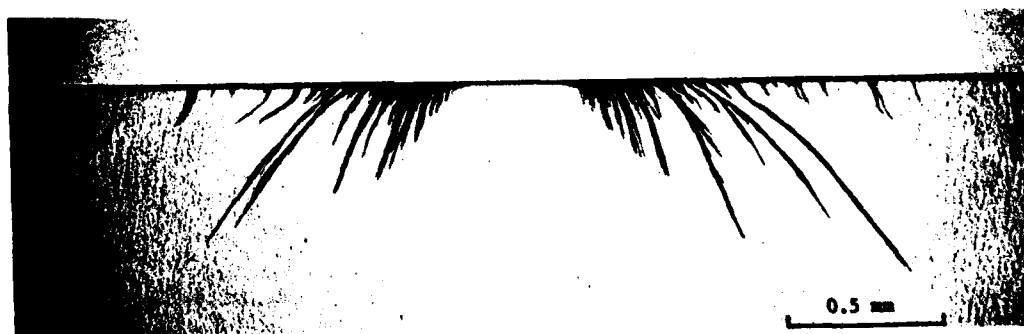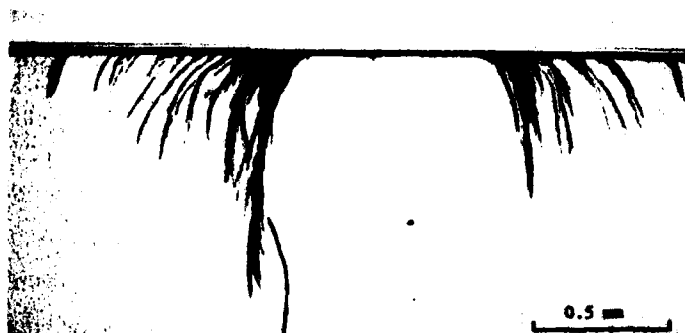
(h) Water drop shot no. 1249 at 582 ms^{-1}.

Figure 3.13.   (continued)

Measurements of the fracture depths and the radial locations of the dominant Type I and Type II fractures are listed in Table 3.2, however the accuracy with which these identifications can be made is not too high for the Type II fractures. When the water jet measurements are compared with those for spherical drops, favorable agreement is only achieved for the 300 ms^{-1} impact. The data for the higher velocities does not compare in magnitude or follow the trend in the data for spherical drop impacts presented in Fig. 3.2 to 3.4: the values for Type I fractures tend to agree more closely than those associated with the ill-defined Type II fractures for water jet impacts.

The observation concerning the extent of the subsurface fractures based on microscopic examination of the intact water jet impacted specimens using transmitted light illumination is clearly substantiated by the subsurface fracture patterns in Fig. 3.13. A sizable degree of asymmetry is also noted in the higher velocity water jet impact subsurface fracture patterns.

3.3   NYLON BEAD IMPACTS ON ZINC SULFIDE

An alternative to liquid impacts on materials is the use of soft solid materials. The potential for this approach as a suitable simulation procedure was suggested in the preliminary investigation reported by Adler and James (1979).

A test matrix was designed for the velocity range from 300 to 600 ms^{-1} using nylon beads. Since no simple basis was available for establishing a comparison between the extent of the damage produced by nylon beads and that due to 2 mm water drops, nylon beads with nominal diameters of 1.2, 1.6, and 2.0 mm were used in these experiments. The liquid drop impact facility was used in the following manner. The nylon beads were suspended on a human hair and positioned so they would impact the center of the specimen. The procedure was then identical to that used for water drop collisions. The powder gun is fired and the same

50

records are made of the impact event as for a water drop impact. Traces
of the hair in the surface fracture pattern are seen at points away from
the central damage zone, however the amount of damage is negligible with
respect to that due to the nylon bead.

A selection of some of the better impacts are shown in Fig. 3.14.
Several effects were noted with respect to the nylon bead collisions,
however the subsurface fracture patterns as seen in Fig. 3.15 are quite
similar to those for water. For several reasons which will be explained
it was difficult to establish empirical correlations between the extent
of the subsurface damage due to nylon bead impacts and that due to water
drops as was initially thought to be possible.

The nylon formulation from which the beads were made appeared to
be moderately crystalline. The mode of deformation during the impact
process tended to be locally nonuniform. This lack of internal uniformity
generally resulted in a highly irregular central undamaged zone which
also led to local perturbation in the circumferential fracture pattern
in the vicinity of the boundary of the central undamaged zone. Although
these initial distortions were present, the subsurface fracture patterns
did not seem to be overly sensitive to their occurrence. In addition it
was found that a negligible to sparse amount of damage would result if
the impact conditions were not severe enough. For these conditions the
nylon bead would rebound from the surface as a solid without flowing over
the surface in the manner of a liquid. Thus several of the test condi-
tions in the test matrix did not produce usable data. Even though there
was significant disruption in the region surrounding the central undam-
aged zone, the far field circumferential fractures were often quite
uniformly distributed and concentric.

Referring to Fig. 3.14, it is observed that the 1.2 mm nylon
bead impact at 602 ms^{-1} does show evidence for the initiation of radial
fractures in contrast to the equivalent 2 mm water drop impact produced
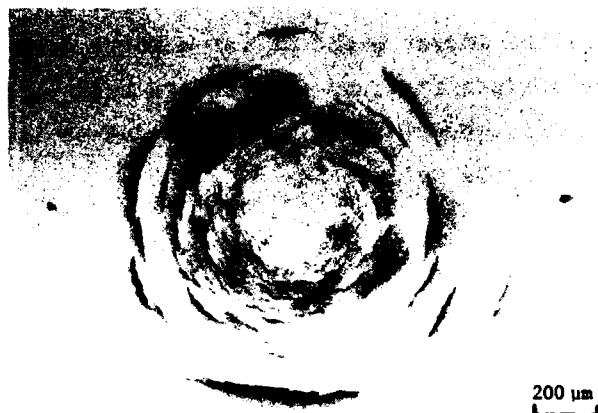
(a) Shot no. 1217b: 1.6 mm nylon bead at 372 ms^{-1}
(transmitted light illumination).

(b) Shot no. 1215: 1.96 mm nylon bead at 381 ms^{-1}
(transmitted light illumination).

Figure 3.14. Overview of nylon bead impacts on zinc sulfide.

(c) Shot no. 1214: 1.2 mm nylon bead at 602 ms^{-1}
(transmitted light illumination).
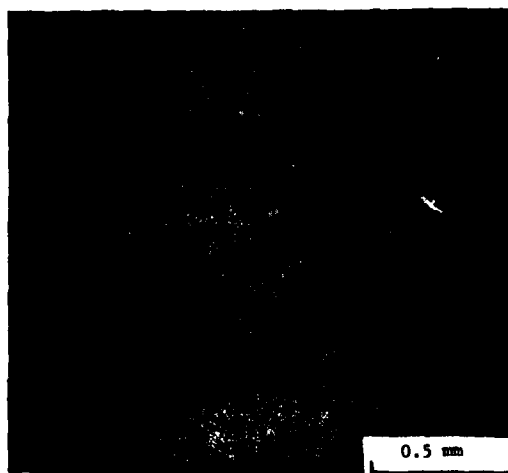
(d) Shot no. 1214: 1.2 mm nylon bead at 602 ms^{-1}
(reflected light illumination).

Figure 3.14.   (continued)

(a) Shot no. 1217b: 1.6 mm nylon bead at 372 ms^{-1}.
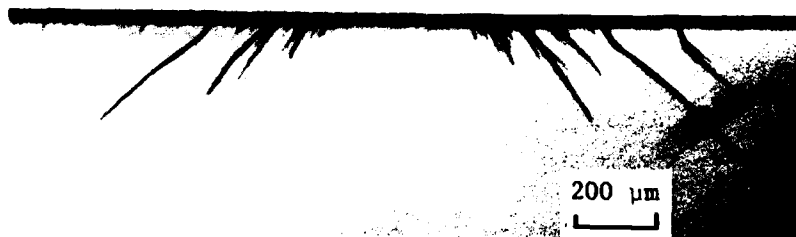
(b) Shot no. 1215: 1.96 mm nylon bead at 381 ms^{-1}.

(c) Shot no. 1200: water drop impact at 354 ms^{-1}.

Figure 3.15.   Comparison of subsurface fractures due to nylon
                bead impacts with spherical water drop impacts
                for comparable impact conditions on zinc sulfide.
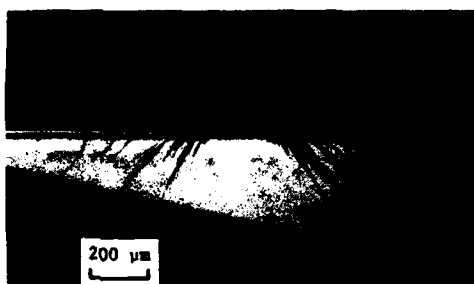
(d) Shot no. 1213: 1.66 mm nylon bead at 549 ms^{-1}.

(e) Shot no. 1235: water drop impact at 540 ms^{-1}.

Figure 3.15. (continued)

(f) Shot no. 1214b: 1.2 mm nylon bead at 602 ms^{-1}.

(g) Shot no. 1249: water drop impact at 582 ms^{-1}.

Figure 3.15.   (continued)

56

by a water jet (Fig. 3.11). The cross sections for nylon bead impacts in Fig. 3.15 also display fractures which can be categorized as Type I or Type II to the same extent as for water drop impacts. The Type II fractures are dominant with respect to fracture depth at the lower impact velocities, but the Type I fractures become dominant at the higher velocities. This trend corresponds to the observations for water drop collisions. The increase in the radial location of the dominant Type II fracture above 550 ms^{-1} is also evident in the cross sections in Fig. 3.15 and in the data summarized in Table 3.3.

An effort was made to measure the diameters of the central undamaged zones. These values, in several instances highly approximate, are tabulated in Table 3.3. Profilometer traces of some of the more uniform nylon bead impacts are shown in Fig. 3.16. The fairly large surface fracture displacements, about 0.3 μm, which occur in the vicinity of the central undamaged zone, are particularly striking. Some tendency can be discerned in the mean surface profile for the existence of a depressed annulus surrounding the central zone found to be characteristic of spherical water drop collisions, but the depressed annulus is not as evident as for the water drop impact conditions.

This investigation provides support for the existence of a meaningful correspondence between nylon bead and water drop impact damage. The similarity in both the qualitative and quantitative features of the impact damage can be improved if the beads were made from a much less crystalline nylon formulation or possibly from other soft, amorphous polymers.

Table 3.3. Experimental Measurements of Nylon Bead
Impact Damage Parameters for Zinc Sulfide.

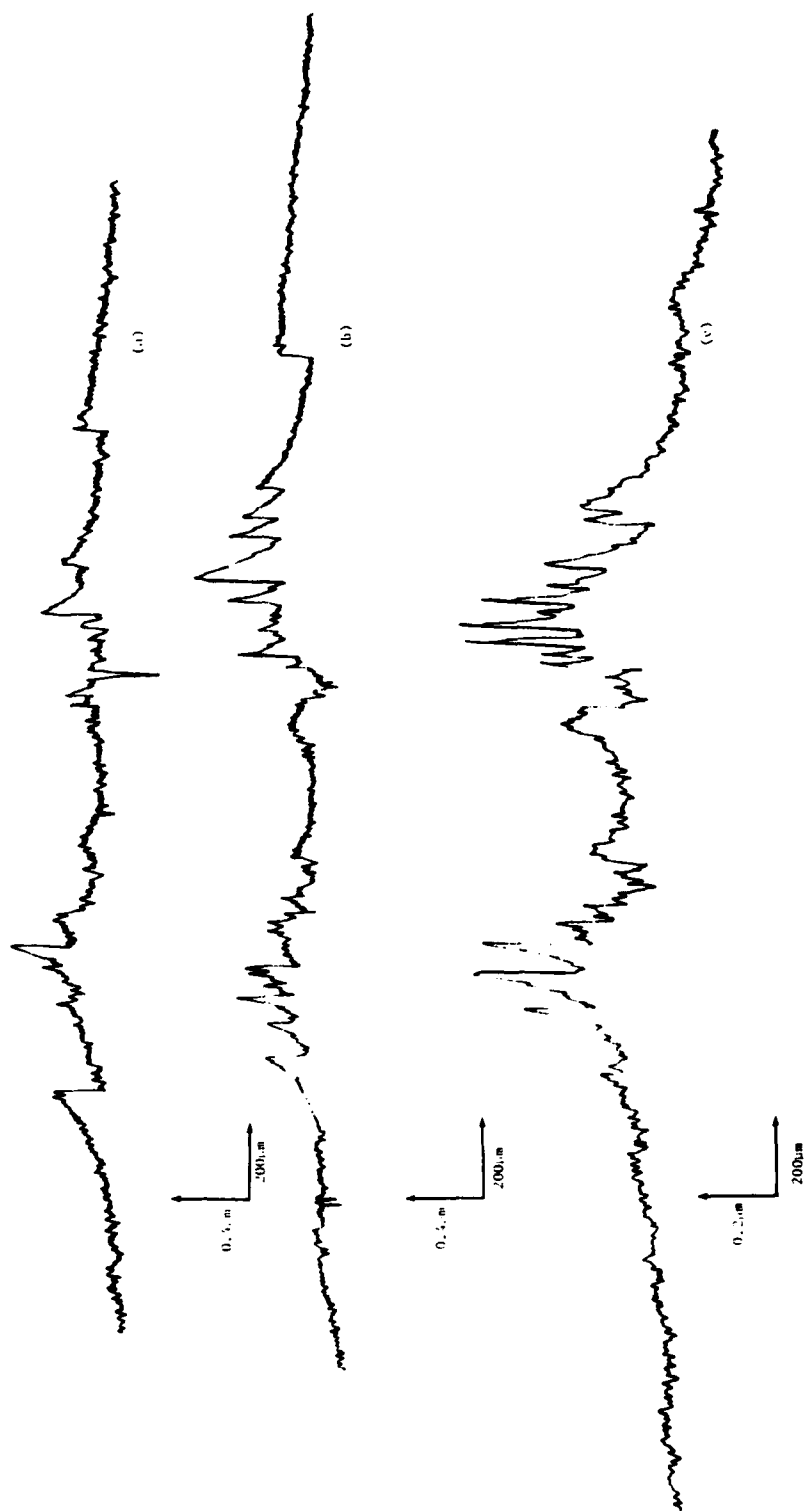| Shot No.	Impact Velocity (ms⁻¹)	Bead Diameter (mm)	Central Undamaged Zone Diameter (mm)	Remarks	Type I Fracture Left Location (mm)	Depth (mm)	Type I Fracture Right Location (mm)	Depth (mm)	Type II Fractures Left Location (mm)	Depth (mm)	Type II Fractures Right Location (mm)	Depth (mm)
1216a	363	1.2	—	Incomplete rings								
1216b		1.2	0.21-.24	Segmented rings								
1217a	372	1.6	—	Segmented rings								
1217b		1.6	0.24	Not coherent, good far field	0.24	0.09	0.30	0.11	0.39	0.20	0.36	0.13
1215	381	1.96	.24		.29	.22	.27	.23	.43	.25	.46	.34
1209a	384	1.19	—	Incomplete rings								
1209b		1.58	—	Difficult to define, good far field								
1209c		1.96	.29	Not coherent, good far field								
1210a	390	1.19	—	Incomplete rings								
1210b		1.58	—	Difficult to define, poor far field								
1210c		1.94	.30	Not coherent, acceptable far field	.33	.58	.35	.68	.87	.304	.51	.33
1253	499	1.6	.35	Not coherent, good far field	.38	.48	.22	.48	.51	.43	.48	.61
1218a	549	1.23		Not coherent, good far field	.25	.435	.31	.71	.51	.43	.81	
1218b		1.57	—									
1213	549	1.66	—	Fair, good far field								
1211	555	1.2	.32									
1212	580	2.0		Highly elongated center								
1252	591	1.6		Boundary irregular, good far field								
1214a	602	1.2	.35	Boundary irregular, good far field	.35	.61	.38	.76	.96	.33	1.06	.28
1214b		1.2	.35		.30	.58	.38	.66	.71	.49	0.81	.23

58

Figure 3.16. Surface profiles through centers of nylon bead impacts on zinc sulfide. (a) Shot no. 1253: 1.6 mm nylon bead at 499 ms^{-1}; (b) Shot no. 1218b: 1.57 mm nylon bead at 549 ms^{-1}; (c) Shot no. 1214b: 1.2 mm nylon bead at 602 ms^{-1}.

59

3.4   WATER DROP IMPACTS ON CALCIUM FLUORIDE

Both single crystals and polycrystals of calcium fluoride (CaF_2) were investigated for their response to water drop impacts in the velocity range from 457 to 536 ms^{-1}. A grain size variation is present in the polycrystalline CaF_2, however different processing procedures were used in fabricating these materials.

3.4.1 Material Description

Single crystal CaF_2 was investigated as a baseline material. Specimens with the impact face in the (100) and (111) planes were prepared by mechanical polishing and chemically etching with aqua regia. A micrograph of the dislocation etched (100) face prior to water drop impact is shown in Fig. 3.17. The remainder of the CaF_2 investigated are polycrystalline.

Annealed *CaF₂* with very large grains (approximately 5 mm) was investigated as a first modification of the single crystal condition. This polycrystalline material is produced by Harshaw Chemical Co. and is sold under the trade name Polytran. The grains are of varied sizes and random orientations.

A material with smaller grain size than the Polytran was obtained from the Eastman Kodak Co. This material is sold under the trade name Irtran 3 and is prepared by hot press sintering a CaF_2 powder. Irtran 3 has a grain size of approximately 100 microns and a reasonably low dislocation density within the grains. A dislocation etched surface is shown in Fig. 3.18. The Irtran material contains many inclusions such that when viewed with the naked eye it appears dirty when compared to the single crystal or the pressed-forged materials which will be discussed next.
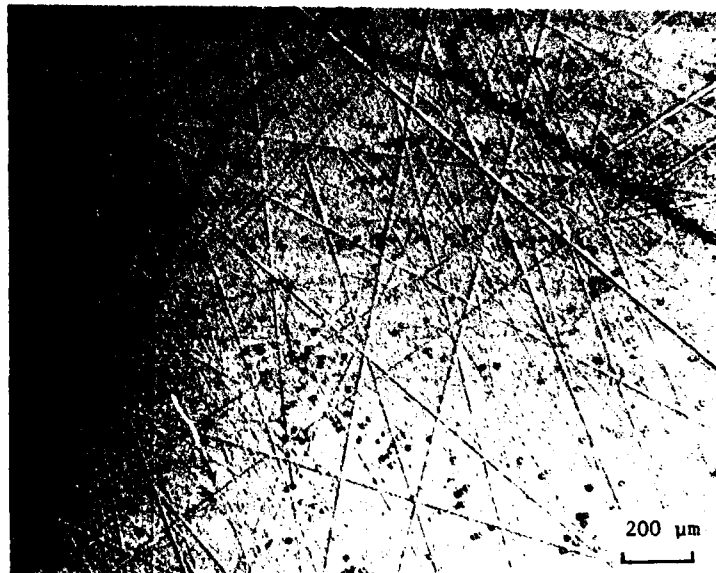
Figure 3.17. Dislocation etched (100) face of single crystal
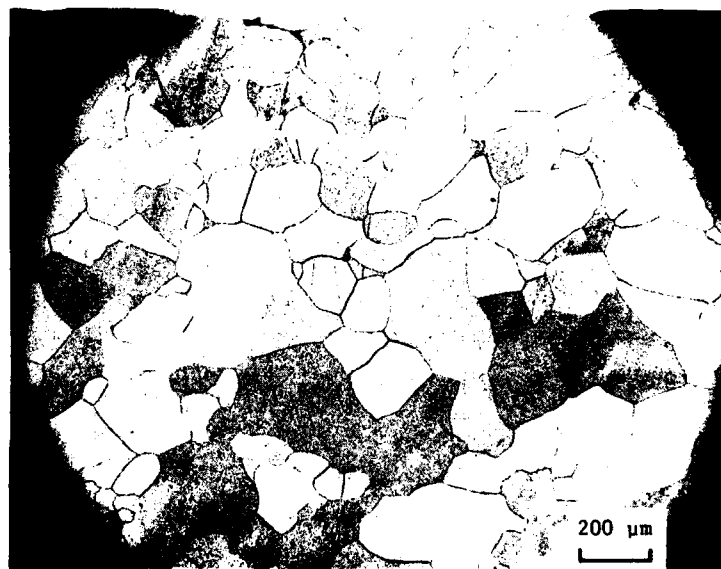CaF$_2$ prepared for water drop impingement.

Figure 3.18. Etched surface of hot-pressed CaF$_2$.

61

Isostatic press-forged CaF_2 discs were obtained from the Air
Force Materials Laboratory. Specimens were prepared from 16 mm diameter
cylinders cored from larger discs. The faces on the cylindrical speci-
mens were parallel to the faces of the forging. One face was mechanically
polished and chemically etched. A micrograph of a prepared surface is
shown in Fig. 3.19. As can be seen from Fig. 3.19 the press-forged mate-
rial does not have a well-defined microstructure nor discernible grains.
The local variations in grain structure (texture) which are present in
this material are shown in Fig. 3.20 at a lower magnification.

Anderson, et al., (1979), describe the processing details for the
press-forged material from single crystal blanks. A high degree of cry-
stallographic orientation is observed between all subgrains (referred to
as subgrains here because the materials investigated did not have a dis-
tinct grain size as noted above). They found during fracture tests that
the specimens would fail macroscopically as if on a cleavage plane. The
pseudo cleavage plane coincides with the average of the individual cleav-
age planes of the subgrains. Since the subgrains were highly oriented
the material fractured in the manner of a single crystal.

3.4.2 Results

Water drop impacts on the single crystal specimens produced
cleavage fractures on the {111} planes. Limited slip deformations
on the [110] {100} slip system were also observed. Both the crystal-
lographic nature of the fractures and the dislocation etched slip bands
are visible in Fig. 3.21 and 3.22. The fracture pattern below the surface
is characteristic of the impact face for both the (111) and (100) oriented
crystals. These fracture patterns are illustrated in Fig. 3.23 a and b.

For both the (111) and (100) oriented impact faces it was verified
that the fractures are predominantly on the {111} planes which intersect
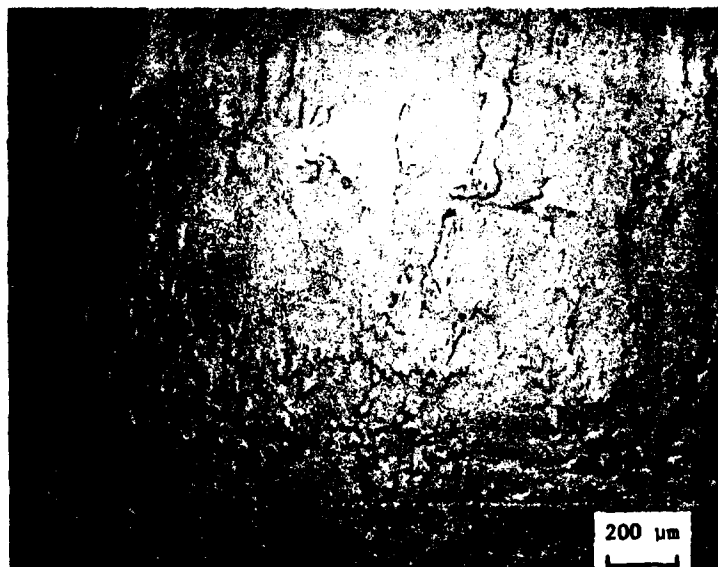the impact face at angles of 70.5° and 54.74° for (111) and (100) oriented

Figure 3.19. Dislocation etched mechanically polished surface of isostatic press-forged CaF_2 as prepared for water drop impingement.

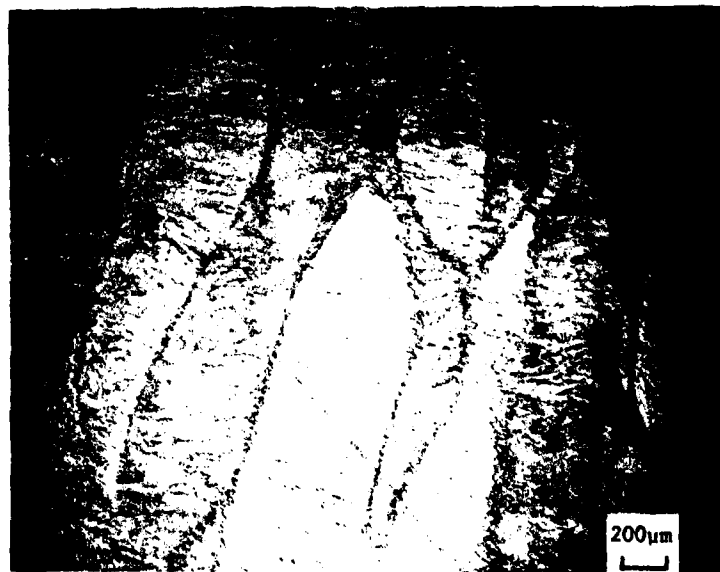Figure 3.20. An example of the texture seen in the microstructure of press-forged CaF_2.

Figure 3.21. Etched water drop impacted surface of (111) CaF_2. Impact velocity is 520 ms^{-1}. Arrows indicate cross section shown in Fig. 3.23a.
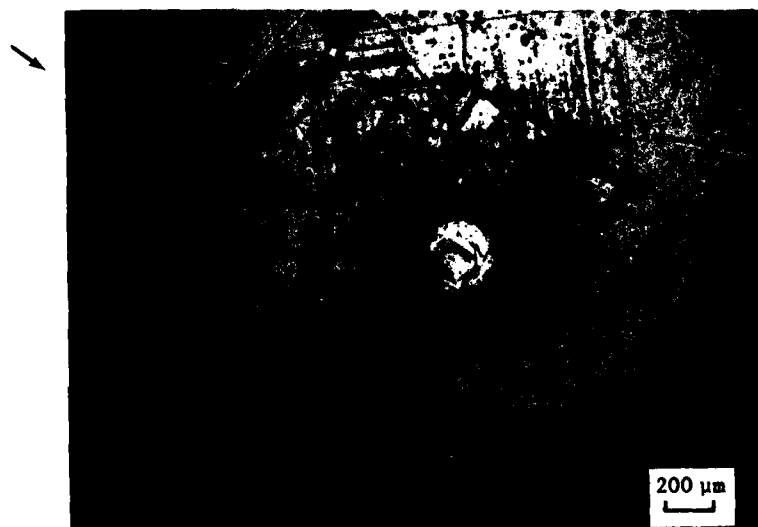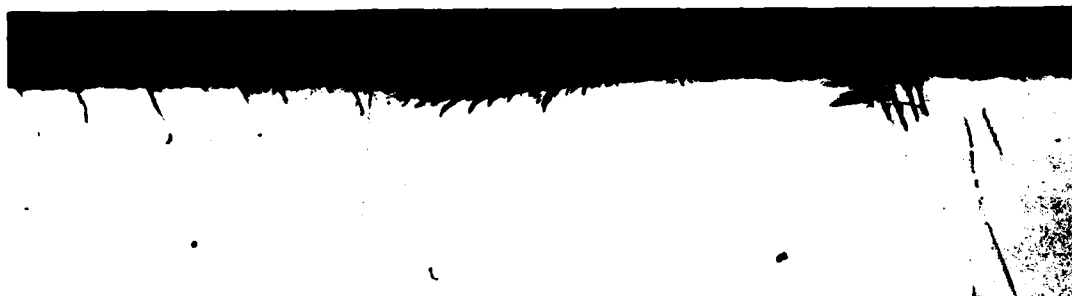

Figure 3.22. Etched water drop impacted surface of (100) CaF_2. Impact velocity is 529 ms^{-1}. Arrows indicate cross section shown in Fig. 3.23b.

(a)   (111) CaF$_2$

(b)   (100) CaF$_2$

Figure 3.23.   Characteristic subsurface fracture patterns for
single crystal CaF$_2$. Both cross sections are on
the (110) plane which passes through the center
of impact.

specimens, respectively. There are three {111} planes intersecting a (111) impact face and four {111} planes intersecting a (100) oriented impact face. These geometries can be seen in Fig. 3.21 and 3.22. The fractures which do not tend to follow the {111} cleavage planes can be seen as radial fractures at the corners of the primary fracture arrays on the (100) oriented specimen (Fig. 3.22) and as a large ragged chip on one of the three radial arms of the (111) oriented impact specimen seen in Fig. 3.21. These non {111} cleavage plane fractures do not appear in water drop impacts at lower velocities (Adler and James, 1979).

In order to reveal dislocations the specimens were etched in aqua regia for 1 min. at 20°C. The etchant not only reveals dislocations but also accentuates the intersection of fine fractures with the surface. Very tightly closed and fine fractures are also made visible. Dislocation etch pits and slip bands due to the water drop collisions can be seen in both the (100) and (111) oriented specimens. Although single crystal CaF_2 does exhibit dislocation slip during water drop impact, slip is much less pronounced in CaF_2 than in MgO (Adler and James, 1979). Conversely MgO exhibits much shallower and less damaging fractures than CaF_2.

To determine the influence of grain boundaries on impact damage, a specimen of Harshaw Polytran was impacted with the result shown in Fig. 3.24. The impact in Fig.3.24 occurred entirely within a single grain with the impacted surface closely oriented to a (100) plane. The similarity between the (100) single crystal impact and the Polytran impact is readily apparent.

A macroscopically noncrystallographic fracture pattern resulted for water drop impacts on Irtran 3: in fact the fracture pattern looks like the fracture patterns produced in ZnS. Although the damage pattern appears isotropic on a macroscopic scale, on a microscopic scale the fractures are still very much affected by the crystallography. Figure 3.25

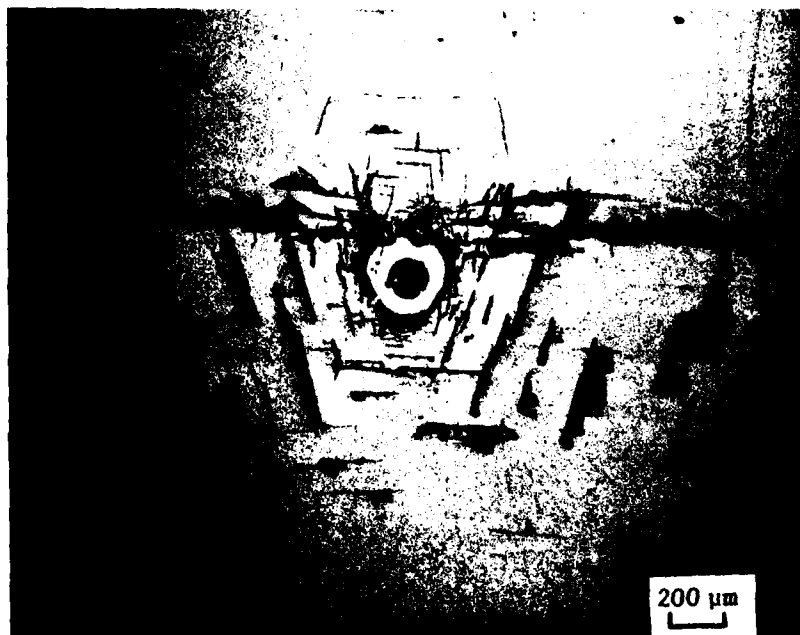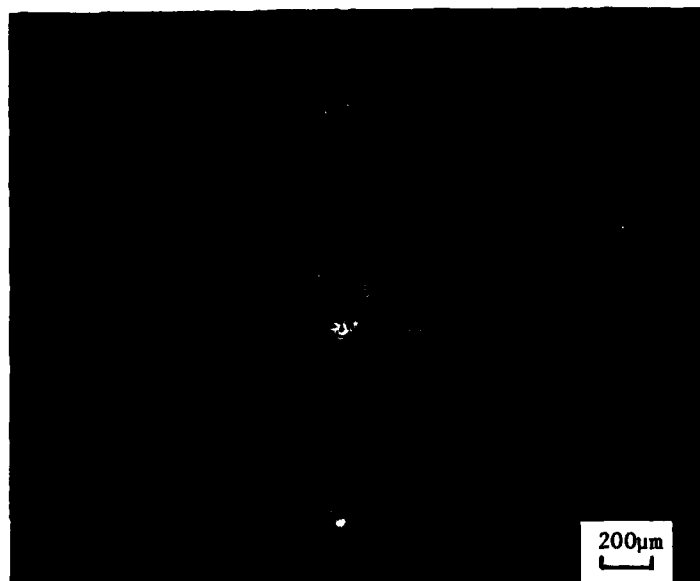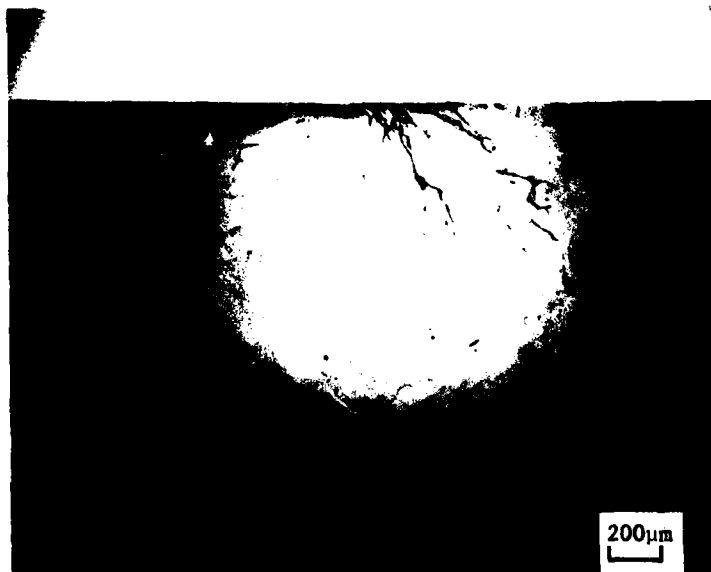Figure 3.24. Water drop impact damage on very large
grain CaF$_2$. Impact velocity is 518 ms^{-1}.

(a) Etched impact face.

(b) Etched cross section.

Figure 3.25. Water drop impact damage on hot pressed CaF_2. Impact velocity is 518 ms^{-1}.

displays the impact face and a cross section of the fractures due to a water drop impact at 518 ms^{-1}. Within individual grains the fractures tend to almost always follow the {111} cleavage planes of the grain. In addition to the small-scale cleavage plane influence, the grain boundaries also influence the form of the fracture patterns. The fracture trajectories are affected by different factors in different regions of the impact volume. Beyond moderate distances from the impact site grain boundaries are the preferred fracture path. The course of the fracture trajectories in this region can be seen in the enlarged cross section in Fig. 3.26. In addition to aiding and/or altering the fractures in this region as observed in cross sectional views, the grain boundaries appear to enhance the extent of damage visible on the impact surface. Fractures are visible on the surface at significantly greater radii than were observed in either the single crystal specimens, Polytran, or the press-forged material. These circumferential surface fractures surrounding the impact site are visible in Fig. 3.27.

At higher impact velocities (546 ms^{-1}) Irtran 3 responds qualitatively in the same manner as described above but in addition individual grains and/or groups of grains are removed from the surface (see Fig. 3.28).

The impact fracture patterns for press-forged CaF$_2$ are shown in Fig. 3.29. A strong tendency for crystallographic geometry in the fracture patterns was observed. The impacts can be loosely organized into three classes depending on the impact fracture pattern. The three general categories based on the average orientation of the impact face are: the impact face is oriented close to a (100) (Fig. 3.29a), the impact face is oriented close to a (111) plane (Fig. 3.29b), and the impact face is oriented intermediate to (100) and (111) planes (Fig. 3.29c and d). As previously noted the press forged material has a highly oriented microstructure and therefore has "quasi" cleavage planes due to the close coincidence of {111} cleavage planes in adjacent subgrains. The damage

69
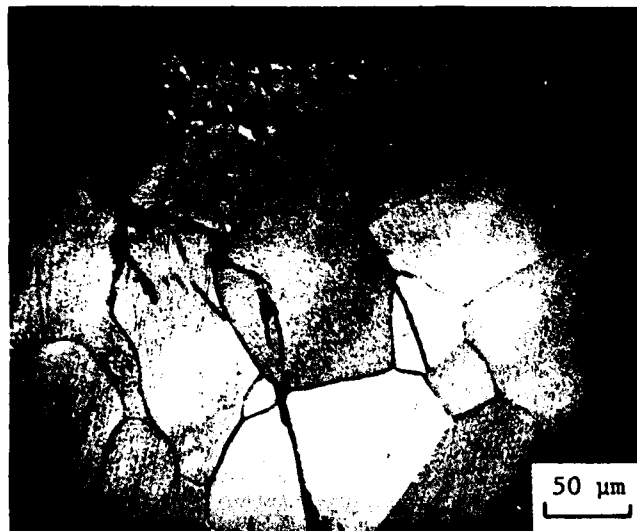
Figure 3.26. Detail of fracture trajectories
seen in Fig. 3.25b.

Figure 3.27. Circumferential fractures present on the specimen
in Fig. 3.25a as seen when viewed in transmitted
illumination. Note the large radial distances at
which circumferential fractures are found.
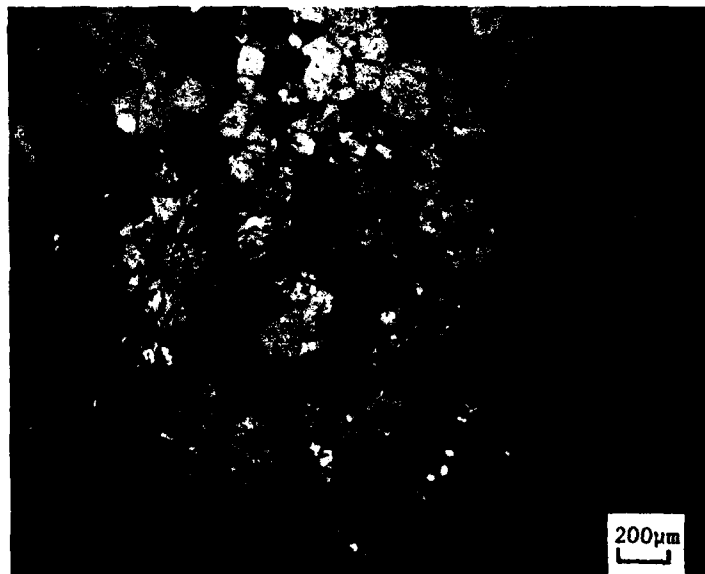
Figure 3.28. Surface grain removal for hot-pressed CaF_2
due to water drop impingement at 546 ms^{-1}.

71
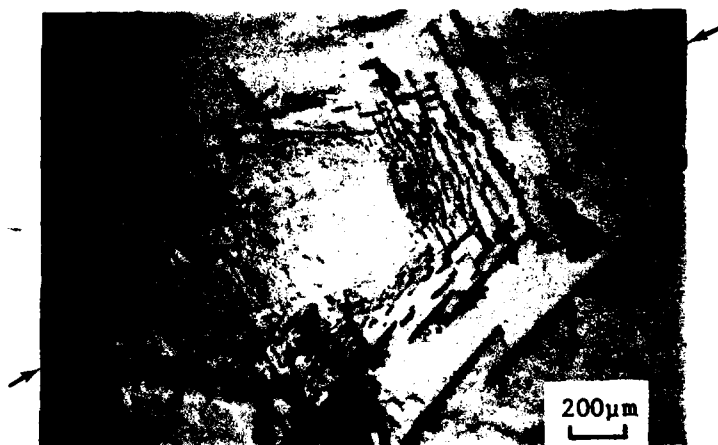
(a) Impact face oriented close to a {100} orientation (at 495 ms^{-1}).
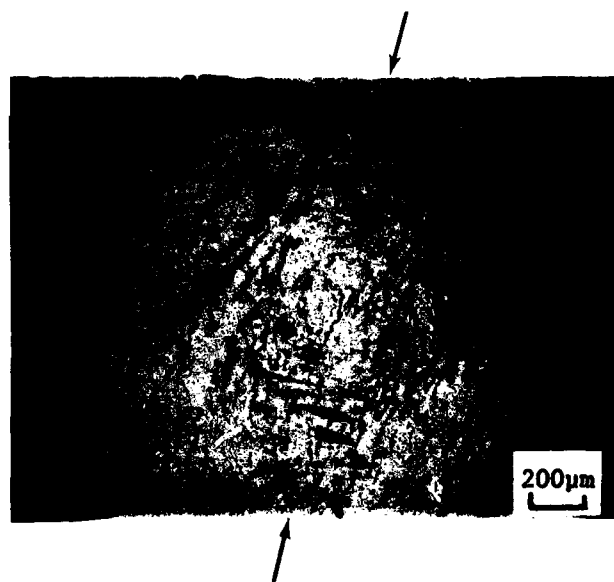
(b) Impact face oriented close to a {111} orientation (at 457 ms^{-1}).

Figure 3.29. Water drop impact damage on press-forged CaF$_2$.

(c) Impact face oriented intermediate to a {111}
    and {100} orientation (at 502 ms^{-1}).
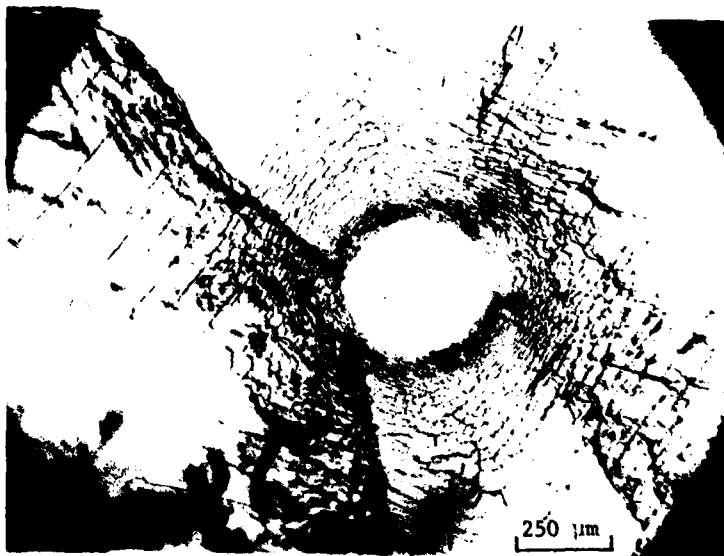
(d) Impact face oriented a second intermediate
    orientation (at 530 ms^{-1}).

Figure 3.29.   (continued)

73

then reflects the crystallography of the average orientation of the surface impacted. The similarity of the damage in Fig. 3.29a to that in Fig. 3.22 and 3.24 illustrates this point. In addition to having a crystallographic impact fracture pattern on the impact face the press-forged material also fractures on the average cleavage planes below the surface. The subsurface fracture pattern corresponding to the impact in Fig. 3.29a is shown in Fig. 3.30. It can be seen from the cross section that the {111} cleavage planes which for a {100} oriented impact Fig. 3.23b) intersect the surface at 54° are now oriented such that one set of {111} planes is approximately perpendicular to the surface and the other inclined at 18°. The three axis pattern of an impact on a {111} oriented surface (Fig. 3.21) is recognizable in the fracture pattern of the specimen whose face was oriented close to {111} (Fig. 3.29b). The subsurface fractures for this impact (see Fig. 3.31) do not show the exclusive preference for the average {111} cleavage planes as did the impact on the specimen whose orientation was close to {100}. The general lack of fractures on the average cleavage planes may be due to their unfavorable orientation to the transient stresses passing through this region. The fractures visible in cross section for the impact shown in Fig. 3.29c (orientation intermediate to {100} and {111}) are shown in Fig. 3.32.
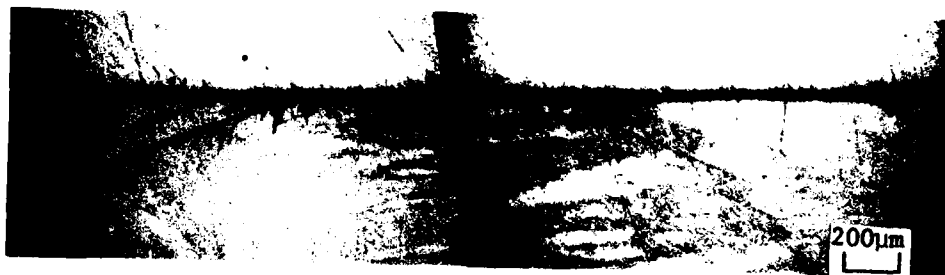
Figure 3.30. Subsurface fracture pattern for a water drop
collision on press-forged CaF_2 with the impact
face close to a {100} plane. This section is
denoted by a pair of arrows on Fig. 3.29a.

Figure 3.31. Subsurface fracture pattern for a water drop
collision on press-forged CaF_2 with the impact
face close to a {111} plane. This section is
denoted by a pair of arrows on Fig. 3.29b.

75

200 μm
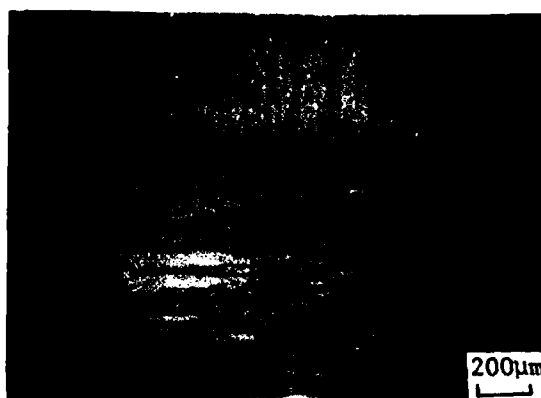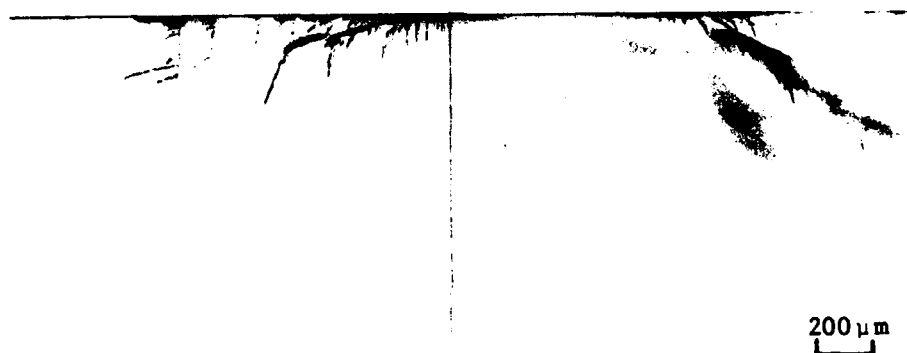
Figure 3.32. Subsurface fracture due to a water drop impact on press-forged CaF_2 with the impact face oriented intermediate to a {100} and {111} orientation. This section is denoted by a pair of arrows on Fig. 3.29c.

4.0   DISCUSSION AND CONCLUSIONS

Spherical water drop impact damage on CVD zinc sulfide has been investigated in considerable depth. Measurements of the identifiable features of the impact damage have been made which provide a data base for this material at impact velocities from 200 to 825 ms^{-1}. The ideal spherical geometry of the water drops prior to impingement on a homogeneous, isotropic target material makes possible direct correlations between the loading imparted to the target and the response of the target.

The indirect evidence provided by the form of the deformation of the contact zone supports the peak pressure distributions obtained from experiments and from finite difference computational models whereby the peak pressure occurs in the vicinity of the periphery of the contact zone and the maximum peak pressure occurs away from the axis of symmetry. Consideration of the computed form of the spatially and temporally varying pressure distribution leads to the hypothesis that the average pressure distribution is fairly uniform with a magnitude close to the value of the water hammer pressure. This observation, along with the fact that the kinematics of the initial stages of the water drop collision process are adequately represented by the geometric relation for a compressible water drop impacting a rigid surface, is consistent with the assumptions made regarding the surface pressure distribution in Blowers' analysis (Blowers, 1969) for evaluating the elastic stresses in the target material prior to the onset of lateral outflow jetting. Comparisons based on the limited published results from finite difference computations with the results from Blowers' analysis have also been made and are in reasonable agreement. Blowers' analysis may therefore be regarded as a viable approach for understanding the response of the target to water drop impingement.

The experimental fracture response of the target can therefore be interpreted in terms of the transient stress distributions readily available from Blowers' analysis. An initial effort in this direction

77

has shown a very close correlation with the onset of circumferential
fracturing outside the central undamaged zone and the radial tensile
stresses which develop prior to and after separation of the shear wave
from the contact zone. This analysis has provided an explanation for
the general character of the Type I and Type II fractures identified on
cross sectioned water drop impacted specimens as seen in Fig. 2.2, 3.13,
and 3.15. More detailed comparisons between the experimental measure-
ments and the calculated results will be made now that there is a
rationale for these comparisons.

Although there is considerable statistical variation in the
fractures created by the water drop impact, measurements of the location
and depth of the largest Type I and Type II fractures viewed in cross
section did provide reasonably consistent data. The magnitudes of the
average fracture depths for the Type I and Type II fractures in Fig. 3.3
and 3.4 are quite similar except for the most severe collisions. The
fracture depths increase monotonically with impact velocity as would be
expected. The interesting result however is the dramatic increase in
the radial locations of the Type II fractures at an impact velocity of
550 ms^{-1} (Fig. 3.2). The magnitude of the transition is considerably
larger than the inherent experimental error in the identification and
measurement of these radial distances. The observed transition corre-
sponds to the onset of random radial fractures which appear to originate
at intersecting circumferential fracture surfaces usually away from the
central damage zone. Blowers' analysis does indicate that significant
circumferential tensions are present at these approximate locations.
The exact sequence of events taking place and the features at the origin
of these fractures have not been adequately investigated to reach any
conclusions concerning their formation. Horizontal fractures are also
observed below the impact site for the higher velocity impacts as shown
in Fig. 3.8. A horizontal fracture below the impact site was first de-
tected for an impact at 582 ms^{-1}. The horizontal fractures are thought
to be due to rapid elastic recovery of the central region of the impact
which becomes significant for the higher velocity impacts. Uplifting of
the central portion of the damage site by several micrometers is seen on

78

profilometer traces passing through the center of the damage zone. The
variation in the surface profile can be seen in Fig. 3.7 with the char-
acteristic shape at velocities below 600 ms^{-1} being a depressed annular
region surrounding the central undamaged zone.

The general fracture patterns for nylon bead collisions on zinc
sulfide are found to be similar to those due to water drop impacts (Fig.
3.15). The determination of the conditions for which the impact damage
is nearly identical for these two loading conditions is not straightfor-
ward. Better experimental results may be achieved with nylon formula-
tions which are less structured than the one from which the beads used
in the impact experiments were made. Other soft, amorphous polymers may
also be considered for this purpose. The correlation with water drop
impact damage on zinc sulfide does not appear to be a general result
based on preliminary experiments with polymethylmethacrylate and single
crystal magnesium oxide. The classes of materials for which the water
drop/nylon bead correlation is valid remains to be determined.

While the nylon bead collisions were found to have potential for
producing damage comparable to that due to water drop impacts, the damage
on zinc sulfide produced by well-characterized water jets designed to
simulate the effects of small water drop impacts did not display the same
degree of similarity. Differences were observed both in the nature and
extent of the circumferential fracture arrays on the surface of the speci-
mens (Fig. 3.10 and 3.11) and for the subsurface fracture patterns (Fig.
3.13). The general form of the surface profiles observed for water drop,
nylon bead, and water jet impacted zinc sulfide is shown in Fig. 4.1
based on the profilometer traces in Fig. 3.7, 3.12 and 3.16. A definite
distinction is seen to occur in the surface deformation patterns. The
profiles for nylon bead collisions are seen to be much closer in form to
water drop collisions than the water jet impacts. Correspondingly, dif-
ferences would be assumed to be present in the spatial and temporal de-
velopment of the pressure loading conditions. Zinc sulfide appears to

79
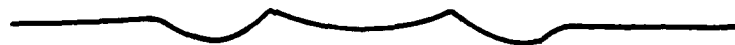
(a) Due to Water Drop Impact.

(b) Due to Nylon Bead Impact.

(c) Due to Water Jet Impact.

Figure 4.1. General form of the profilometer traces for water drop, nylon bead, and water jet impacted zinc sulfide at velocities up to 600 ms^{-1}.

80

be sensitive to the differences between the water drop and water jet impact pressure distributions which have to be significant to produce the large discrepancies in the fracture response seen in Fig. 3.13. No explanation for the observations associated with the water jet will be offered. The correlation between nylon bead and water drop subsurface fracture patterns would also indicate that the unloading phase of the interfacial pressure does not appear to be too significant up to 600 ms^{-1}. The rate of unloading and the spatial pressure distribution will be quite different for a nylon bead compared to a water drop which has no mechanism for recovering its initial form.

Although the radial extent of fractures visible on the impact surface appears to be similar for single crystal, large grain polycrystalline (Polytran), hot pressed and press-forged calcium fluoride, the extent and character of the subsurface fractures are not at all similar. In single crystal and polycrystalline (Polytran) specimens the fractures run rather easily on the cleavage planes: especially when they are favorably oriented. The effect of favorable orientation can be easily seen by comparing the radial extent of fractures visible on the impact face of the (100) and (111) oriented specimens (Fig. 3.21 and 3.22). In the (100) orientation the fractures are more or less concentrated around the central undamaged zone, whereas in the (111) orientation the fractures are arrayed out to great distances along three radial arms. This behavior of the (100) oriented specimens is due to the highly favorable orientation of the four {111} cleavage planes to the (100) impact face. The 54.7° intersection of cleavage planes with the surface closely approximates the fracture paths which form in an isotropic material such as the small grained ZnS considered in Sections 3.1 to 3.3. On the other hand, for the (111) oriented specimens only three cleavage plants intersect the surface and they are oriented at 70.5° to the impact face. The absence of favorably oriented cleavage planes causes numerous shallow fractures to form at great distances: especially where the cleavage planes are oriented down and towards the impact center (see Fig. 3.23a for example). Therefore for a given impact energy to be dissipated by cleavage the fractures must be deeper and/or there must be more of them.

81

Impacts on hot-pressed sintered calcium fluoride produce fractures
which follow the grain boundaries in addition to cleavage plane fractures
in the grains. The grain boundaries seem to produce both nucleation
sites at the surface as well as provide fracture paths within the specimen
away from the impact site. The apparent weakness of the grain boundaries
may be due to the visibly detectable high impurity level in this material.
Since the material is hot-pressed sintered the impurities have ample op-
portunity to diffuse to the grain boundaries and reduce their mechanical
properties. The reduced mechanical properties are demonstrated by both
the observed fracture paths and the observed removal of complete grains
from the surface (Fig. 3.28).

Although the press-forged material appears to show some improvement
in fracture depth attenuation over the single crystal, Polytran, and the
hot-pressed sintered materials, further improvements almost certainly
would result if the highly oriented microstructure could be made iso-
tropic. The highly oriented microstructure allows quasicleavage frac-
tures to propagate only marginally attenuated comparable to a single
crystal. An isotropic microstructure would minimize cleavage type frac-
tures to be dissipated by plastic deformation. This effect is based on
observations made for magnesium oxide where the introduction of numerous
dislocations into the surface prior to impact enhanced energy dissipation
by plastic deformation (dislocation slip) to the extent that the fracture
stress was never exceeded (Adler and James, 1979). The hot-pressed sin-
tered material was somewhat isotropic in its fracture response, but this
failed to produce any increase in its water drop impact resistance be-
cause the grain boundaries provided easy fracture paths in addition to
the cleavage planes within grains.

REFERENCES

W.F. Adler (1977). "Liquid Drop Collisions on Deformable Media,"
J. Materials Science, 12, 1253-1271.

W.F. Adler (1979). "The Mechanics of Liquid Impact," Treatise on
Materials Science and Technology, Volume 16: Materials Ero-
sion (C.M. Preece, ed.), New York: Academic Press, 1979.

W.F. Adler, J.C. Botke, and T.W. James (1979). Response of Infra-
red-Transparent Materials to Raindrop Impacts, Air Force
Materials Laboratory Report AFML-TR-79-4151.

W.F. Adler and S.V. Hooker (1976). Characterization of Trans-
parent Materials for Erosion Resistance, Air Force Materials
Laboratory Report AFML-TR-76-16.

W.F. Adler and T.W. James (1979). Particle Impact Damage in
Ceramics, Technical Report for Office of Naval Research
Contract N00014-76-C-0744 (March 1979).

R.H. Anderson, R.A. Skogman, and H. Vora (1979). "Mechanical and
Optical Properties of Press-forged LiF and CaF$_2$," Optical
Engineering, 18, 602-609.

R.M. Blowers (1969). "On the Response of an Elastic Solid to
Droplet Impact," J. Inst. Maths. Applics., 5, 167-193.

F.P. Bowden and J.H. Brunton (1961). "The Deformation of Solids
by Liquid Impact at Supersonic Speeds," Proc. R. Soc. London,
A263, 433-450.

F.P. Bowden and J.E. Field (1964). "The Brittle Fracture of
Solids by Liquid Impact, by Solid Impact, and by Shock,"
Proc. R. Soc. London, A282, 331-352.

A.G. Evans and R.T. Wilshaw (1976). "Quasi-Static Solid Particle
Damage in Brittle Solids--I. Observations, Analysis and
Implications." Acta Met, 24, 939-956.

J.E. Field, J.J. Camus, D.A. Gorham, and D.G. Rickerby (1976).
High Speed Liquid Impact Studies, Univ. of Cambridge,
DR Mat. Report 203.

J.E. Field, D.A. Gorham, and D.G. Rickerby (1979). "High-Speed
Liquid Jet and Drop Impact on Brittle Targets," Erosion:
Prevention and Useful Applications, ASTM STP 664, (W.F. Adler,
ed.) pp. 298-319. Americal Society for Testing and Materials,
Philadelphia.

J.V. Hackworth and L.H. Kocher (1977). Exploratory Development of Rain Erosion Resistant Infrared Window Materials, Air Force Materials Laboratory Report AFML-TR-77-84.

J.-B.G. Hwang (1975). "The Impact Between a Liquid Drop and an Elastic Half-Space," Ph.D. Thesis, University of Michigan.

R. Kinslow (1974). Rain Impact Damage of Supersonic Radomes, Tennessee Technological University Report No. TTU-ES-74-3 (October 1974).

M.C. Rochester and J.H. Brunton (1979). "Pressure Distribution During Drop Impact," Proc 5th Int. Conf. on Erosion by Solid and Liquid Impact, Cambridge, England (September 1979).

M. Rosenblatt, G.E. Eggum, L.A. DeAngelo, and K.N. Kreyenhagen (1976). Numerical Investigation of Water Drop Erosion Mechanisms in Infrared-Transparent Materials, Air Force Materials Laboratory Report AFML-TR-76-193.

M. Rosenblatt, Y.M. Ito, F.W. Perry, and G.E. Eggum (1977). Analysis of Water Drop Erosion Mechanisms in Infrared-Transparent Materials Using Microphysical Fracture Models, Air Force Materials Laboratory Report AFML TR-77-219.

D.A. Shockey, D.J. Rowcliffe, and K.C. Dao (1977). "Fracture Toughness of CVD ZnS," Topical Report for Office of Naval Research Contract N00014-76-C-0657 (March 1977).

J.M. Wimmer (1979). Mechanical and Physical Properties of Chemically Vapor-Deposited (CVD) Zinc Sulfide, Air Force Materials Laboratory Report AFML-TR-79-4013.